Ultracold rubidium interactions

van Kempen, E.G.M.

Award date:
2002

Ultracold rubidium interactions

Eric van Kempen
January 2002

Aqt/b 02-01

Technische Universiteit Eindhoven
Begeleiding:
Prof. Dr. H.C.W. Beijerinck
Prof. Dr. B.J. Verhaar
Dr. Ir. E.J.D. Vredenbregt

Summary

This thesis reports on both experimental and theoretical work performed in the groups AQT/b and AQT/a respectively.

The experimental work concerns experiments on the road to a Bose-Einstein condensate (BEC) in metastable Ne. This road is first cooling and collecting a large numbers of atoms in a magneto-optical trap (MOT) after which they are transferred to a magnetic trap (MT) in which they are eventually evaporatively cooled. As a guide on this road on this road we need a reliable diagnostic method. Among other methods we use absorption imaging for diagnostics. An absorption imaging system, in which a shadow casted by an atomic cloud (illuminated by a near resonant laser) is registered and analyzed, is tested and found to be usable for the determination of the total number and spatial distribution of atoms in the atomic cloud. The system can also be used for temperature measurement via observation of the time dependence of the expansion of an atomic cloud.

Another step is creating good initial conditions for the start of evaporative cooling. The colder and denser the atomic cloud is to start with, the better. Thereto we tried to make a $\sigma^+\sigma^-$ optical molasses between a MOT and a MT stage. Realization of this cooling method failed due to bad window coatings. Although that problem has now been solved, the pursuit of optical molasses was put to rest in favor of more essential steps.

Essential to reach BEC is a small two-body collisional loss rate for our atomic sample when held in a magnetic trap. Since we use neon in a meta-stable state, Penning ionization plays a role causing the loss rate for two-body collisions to be large. By spin polarizing the atoms, we expect to be able to suppress this ionization process and thereby the loss rate. Measurements indicate an upper limit for the loss rate which would prevent us from reaching BEC. However, these same experimental observations can also be explained by a small two-body loss rate, but a large loss due to spontaneous evaporation from the magnetic trap. This situation provides good changes for the realization of BEC.

The theoretical work consisted in the analysis of interactions between ultracold rubidium atoms. We combine the measured binding energies of four of the most weakly bound rovibrational levels of the $^{87}Rb_2$ molecule with the results of two other recent high-precision rubidium experiments, to obtain exceptionally strong constraints on the atomic interaction parameters in a highly model independent analysis. We are able to deduce dispersion coefficients up to C_{10} and C_{11} and the strength of the exchange interaction. Until now only theoretical values had been available for all these parameters, except C_6. The comparison of ^{85}Rb and ^{87}Rb data, where the two isotopes are related by a mass scaling procedure, plays a crucial role. Due to the mass scaling we are able to deduce the exact number of bound states in the singlet and triplet ^{85}Rb+^{85}Rb and ^{87}Rb+^{87}Rb interaction potentials. With the obtained interaction parameters we are able to predict e.g. scattering lengths and Feshbach resonances with an unprecedented level of accuracy. To demonstrate this we predict a number Feshbach resonances in ^{87}Rb.

Contents

Chapter 1

Introduction

1.1 Bose-Einstein condensation

Let us consider a cloud of bosons. From a quantum-mechanical point of view we can describe these particles as wavepackets with a characteristic dimension of the de Broglie wavelength [1]

$$\lambda_{dB} = \sqrt{\frac{(2\pi\hbar)^2}{mk_BT}}, \tag{1.1}$$

with m the particle's mass, k_B Boltzmann's constant, and T the temperature. As we can see from this equation the quantum-mechanical dimension of a particle increases with decreasing temperature. For low enough temperatures and high enough particle-densities the wavepackets start to overlap. At that point the cloud of bosons undergoes a phase-transition to a so-called Bose-Einstein condensate.

In 1995 Bose-Einstein condensation (BEC) was observed for the first time and has stimulated many research groups around the world to pursue the observation of BEC in samples of elements other than rubidium as well; attempts with the alkalis H, Li, Na, K, and Rb have been successful [2]. Early last year two groups in Paris have been able to Bose condense a sample of metastable He atoms. In Eindhoven we pursue such a condensation for metastable Ne.

The relation between the density and the quantum-mechanical dimension at which this transition occurs is expressed by the following relation [1]

$$\mathcal{D} = n\lambda_{db}^3 \simeq 2.61, \tag{1.2}$$

in which $\mathcal{D}$ is called the phase-space density and n is the particle density. At room temperature (T = 298K) the de Broglie wavelength for ^{20}Ne is $\lambda_{dB} = 5.6 \cdot 10^{-11}$m. At a pressure of 1bar, the phase-space density would be $\mathcal{D} = 4.4 \cdot 10^{-6}$. It is clear that under standard conditions BEC will not take place for ^{20}Ne, so we have to do something special. In chapter 2 an outline is given of some of the steps on the challenging road to BEC.

1.2 This thesis

This thesis consist of two identifiable parts; an experimental and a theoretical part. Although the major part focusses on the analysis of cold interacting Rb atoms (theoretical), equal time has been spent on experimental work. The aim of the experimental part was the realization of a Ne* BEC. This work has been performed in a team of 5 people: the *Gemini*-team of AQT/b under supervision of prof. dr. Beijerinck and is discussed in chapter 2. In the last year this work has shown rapid progress and many new experimental developments have been completed. However, a choice was made not to report on this work in much detail for three reasons. First, due to the present stage of the project much of the experimental effort concerned the development of new experimental techniques limiting the amount of new physics. Secondly, this work has been done on a time-sharing basis, causing much of the work to be completed by others. A final reason is the very limited time in which this report should be completed.

The theoretical part consisted of the continuation of Kokkelmans' work [3] on the interaction of cold Rb atoms and has been performed in the group AQT/a of prof. dr. Verhaar. The theoretical analysis of cold rubidium interactions is discussed in a Physical Review Letter which makes up chapter 4, while chapter 3 provides background information on the analysis presented in the Letter.

Part I

Bose-Einstein condensation in metastable neon

Chapter 2

BEC in metastable Ne

Introduction

To achieve BEC for neon we have to increase the phase-space density to the point of $\mathcal{D}$=2.61. This means that we have to collect a sample of neon atoms and manipulate it in such a way as to cool it as well as compress it, such that $\mathcal{D}$ increases. The most common approach to make a BEC is to first trap and cool atoms in a magnetic-optical trap (MOT) thereafter transferring the trapped cloud to a magnetic trap (MT). Optionally an optical molasses can be created in between the MOT and the MT stage to achieve a lower temperature and higher density after the transfer. The last step is evaporative cooling. These stages will be highlighted below in their respective order.

Before we can discuss the properties of these stages some basic knowledge of the medium used is necessary. In the Eindhoven BEC experiment we use bosonic metastable ^{20}Ne in the 3^3P_2 state (Russel-Saunders notation), which has an internal energy of 16.6eV. This state has a lifetime on the order of 24s. Due to the relatively long lifetime we will from now on call this the (Ne*) 'ground' sate. When excited to the 3^3D_3 state via a $\lambda \approx 640.225$nm (λ the wavelength) photon the system will 'fall back' to the 3^3P_2 state and can therefore be regarded as consisting effectively of two levels, which is desirable for laser cooling. The transition has a linewidth $\Gamma/(2\pi) = 8.2$MHz and an on-resonance saturation intensity $I_0 = 4.08\text{mW/cm}^2$.

2.1 Experimental setup

Some aspects of the experimental setup, necessary for understanding the remaining part of this chapter, will be discussed in this section. An extensive description however is not given here and the reader is referred to [4, 5, 6] for more details. Figure 2.1 shows a schematic view of our setup. Shown are the the MOT laser beams and the MOT magnetic field coils, which will be discussed in section 2.2. In figure 2.1 three diagnostic tools are depicted: a photo-diode, a CCD-camera, and a channeltron.

When the experiment is operated, a cloud of atoms is trapped in the area of intersection of the MOT beams in figure 2.1. The atoms feeding the trap are supplied by a slow atomic beam setup (described in detail by Tempelaars

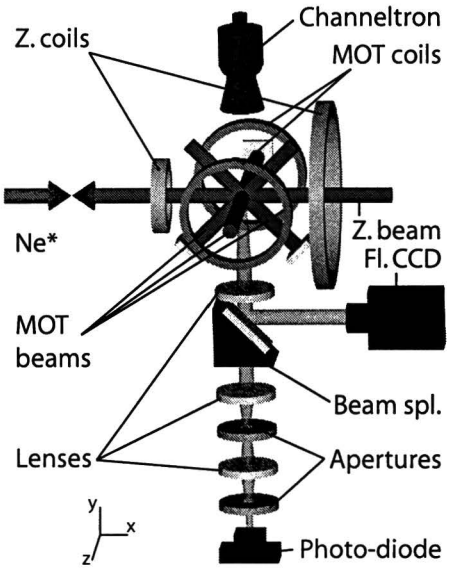

Figure 2.1: Schematic overview of the diagnostic setup. Not indicated in this picture is a light beam used for absorption imaging, directed in the z direction. The lenses and CCD-camera used to obtain the absorption image are behind the depicted setup and are also missing in this picture. So-called compensation coils and coils for the MT are not depicted too. *The 'Z' in the picture refers to Zeeman-slower.*

[4]). When trapped in a MOT (see section 2.2) the atoms will emit (previously absorbed) photons and thus fluoresce. A photodiode is used to measure the power of this fluorescence from which the number of trapped atoms can be derived. To reduce background signal, the fluorescence signal is led through an path of lenses and apertures. On this path a beamsplitter is included which redirects a part of the signal to a CCD camera, the so-called fluorescence camera. This camera signal is send to a TV, for live monitoring, and to a PC with framegrabber to be able to digitize and analyze the signal from which the spatial distribution of atoms within the cloud and the volume of the cloud can be deduced. Above the point of MOT beams intersection, a channeltron is present. It can be used to count e.g. meta-stable atoms or ions which reach the front of the channeltron, situated 4cm above the center of the cloud. A grid is placed in front of the channeltron to discriminate between meta-stables and ions by simply applying a voltage to this grid.

Not shown in figure 2.1 is the setup for absorption imaging. For absorption imaging we need a near resonant light beam to illuminate the could. This light beam propagates in the z direction. The cloud is focussed on a second CCD camera, the so-called absorption-imaging camera, which will register a shadow. This camera is also connected to a PC with framegrabber. Analysis of the image gives the number of atoms as well as the spatial distribution of the cloud. An absorption image is constructed from three images: 1) atomic cloud in light beam; 2) only the light beam; 3) background image. An example of such an

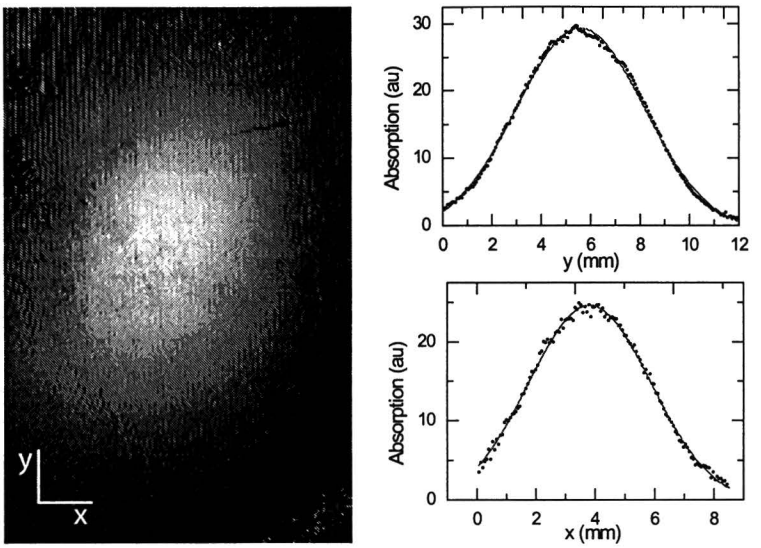

Figure 2.2: Example of an absorption image of the atomic cloud. The picture is taken 2.3ms after the cloud was released from a MOT. It is one of the five images used for the 2.3ms data-points of the graph in figure 2.5. From fitting we find $\sigma_x = 2.1$mm and $\sigma_y = 2.6$mm. The central optical density (correlated to the height of the Gaussian) is found to be 1.92, yielding a total number of atoms $N = 10^9$ (see text). *The image was taken with probe beam detuning* $\delta = \frac{1}{2}\Gamma$.

image is shown in figure 2.2.

Also missing in figure 2.1 are the magnetic field coils for the MT. This magnetic field is generated by a total of fourteen coils in the socalled cloverleaf configuration [5, 6], seven near each MOT coil. Together they produce the desired magnetic field of which the absolute value is shown in figure 2.3. By adjusting the current through the proper coils [6], the steepness of the trap can be changed as is shown by the lower curve in figure 2.3. This steepening of the trap is called compression.

Figure 2.1 also lacks the so-called compensation coils, which produce a homogenous magnetic field at the center of the trap. Each dimension has one pair of Helmholtz coils, so there are in total six compensation coils. They can be operated per pair and compensate for the earth magnetic field (B_{total}=0), hence their name.

2.2 Magneto optical trap (MOT)

Theory

As explained above we have to manipulate a cloud of Ne* atoms in a highly controllable manner. Therefore a number of atoms is trapped in a so-called magneto-optical trap (MOT). The trapping principle is based on the combination of the presence of a magnetic field and a light field. This trap has to be loaded, which we do with an intense and slow beam of Ne*. The experimental

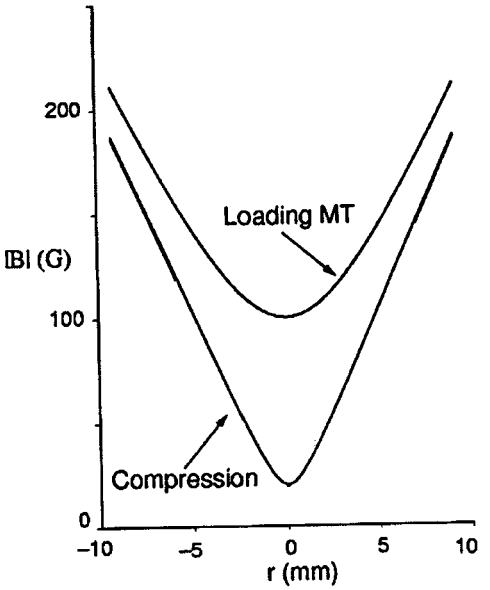

Figure 2.3: Absolute value of the magnetic field as function of the distance to the z-axis. The upper curve corresponds to an uncompressed trap; the lower curve to a compressed one.

setup of this slow beam is described in Tempelaars' thesis [4] and will not be discussed here.

To understand the principle of operation of a MOT we consider a two-level atom with a J=0 groundstate (J the angular momentum quantum number). In zero magnetic field the excited, J=1, state has three degenerate sublevels. A magnetic field $\vec{B}$ splits up these sublevels according to [7]

$$\Delta E = -\vec{\mu} \cdot \vec{B} = g_j m_j \mu_B B, \tag{2.1}$$

with ΔE the energy shift due to $\vec{B}$, $\vec{\mu}$ the atomic magnetic moment, μ_B the Bohr magneton, m_j the projection of the atom's angular momentum along the magnetic field axis, and g_j the Landé factor. Placing this atom in an inhomogeneous magnetic field $\vec{B}(x) = Cx$ (C a positive constant) we obtain an energy splitting as indicated in the lower part of figure 2.4. Next we introduce two oppositely circularly polarized counter propagating laser beams, the σ^+ one propagating in the $+x$ direction (see figure 2.4). These laser beams are both equally red detuned with respect to the $m_j = 0$ transition, i.e. the frequency of the laser is lower than the $m_j = 0$ transition frequency.

If we now picture the atom to the right of the origin, the $m_j = -1$ level will be shifted downwards in energy with respect to the $m_j = 0$ level, while the energy of the $m_j = +1$ level is increased. This implies that an atom on the right of the origin is most in resonance with the σ^- beam and will therefore scatter more photons from this beam than from the σ^+ beam. For an atom on the left

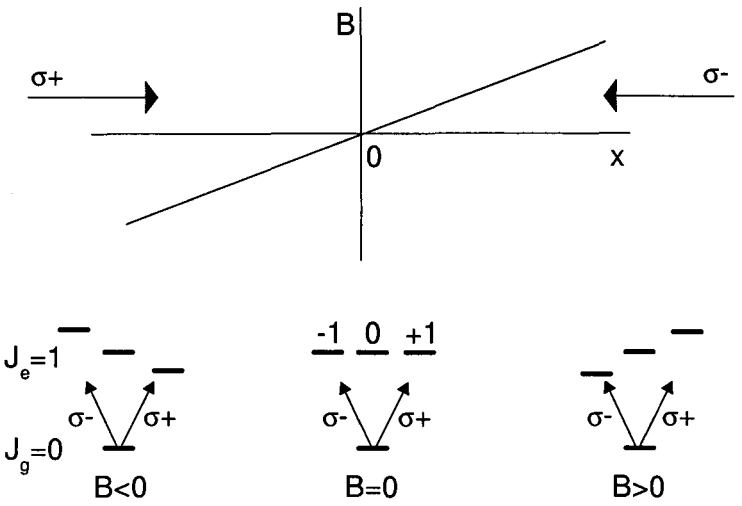

Figure 2.4: Principles of operation for a magneto-optical trap. We have two counter propagating laser beams of opposite circular polarization. An inhomogeneous magnetic field splits the sublevels of the excited state, therefore an atom right of the origin is more resonant with the σ^- light and will therefore absorb more photons from this beam than from the other beam. The opposite holds on the left side, resulting on both sides in a net force directed towards the center.

of the origin the opposite holds. Therefore an atom displaced from the origin will experience a force directed towards the origin. Also cooling of the motional degrees of freedom occurs due to the mechanism explained in section 2.3.

Experimental

To determine the temperature and the total number of atoms in the MOT we implemented a method called absorption imaging. If we want to measure e.g. the temperature of the MOT, we 'release' the atomic cloud and let it expand. By taking images at different times we can measure the expansion versus time. Because we use absorption imaging, taking an image disturbs the cloud such that we cannot take multiple images of one and the same cloud for reliable determination of the temperature. What we do is to make a new MOT cloud for each image taken. That means that a high reproducibility is desired. To reduce errors due to irreproducibility, several images are taken for the same delay. The image is taken with a CCD camera, which is connected to a PC. With the aid of the PC we determine the size of the cloud by fitting the absorption profile with a 2D-Gaussian.

In figure 2.5 we see the diameter of an expanding atomic cloud released from a typical MOT. Each point corresponds to the average of five measurements (7x5 measurements are performed). The probe beam used to make the image has a saturation parameter $s = 0.03$ and a duration of τ=50μs, which is chosen such that few photons are being scattered to avoid disturbance of the image. From the data represented in figure 2.5 we can deduce the temperature by

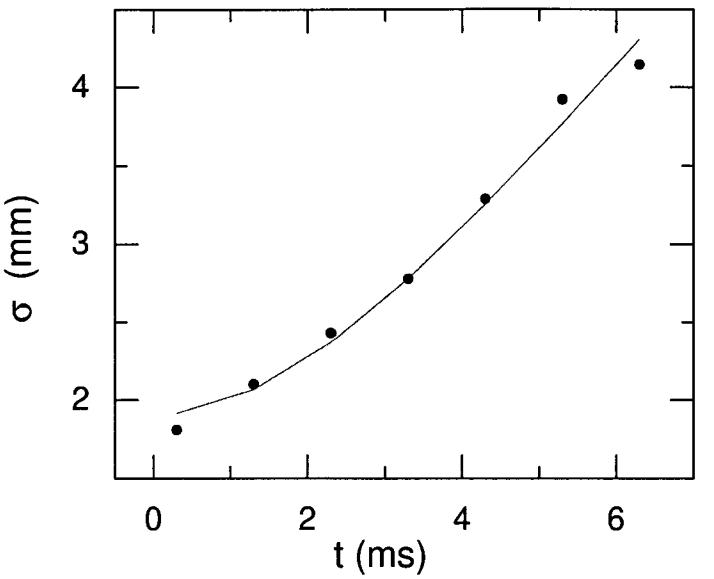

Figure 2.5: Horizontal dimension (rms radius) of an atomic cloud released from a MOT at $t = 0$. The density profile for an image is fitted by $n_0 \exp\{-x_i^2/(2\sigma_i^2)\}$ (see figure 2.2) and each depicted point is the average of five images. The fitted curve (in this picture) obeys $\sigma^2(t) = \sigma_0^2 + k_B T t^2/m$, with σ_0=1.91(8)mm and T=0.90(5)mK. *In this graph the temperature in the y direction is depicted.*

fitting the rms radii of the cloud with $\sigma^2(t) = \sigma_0^2 + k_B T t^2/m$, in which m is the mass of the atoms, k_B Boltzmann's constant, t the expansion time, T the temperature, and σ_0 the rms radius of the cloud at time of release ($t = 0$). In the example of figure 2.5 we find a temperature T=0.90(5)mK, which is a typical temperature for the atoms. From the dimensions of the cloud and its optical density, $\mathcal{OD} = \sigma_A \int_{-\infty}^{\infty} n(\vec{r})\mathrm{d}z$ ($\sigma_A = 3\lambda^2/2\pi$ the absorption cross-section, and n the particle density), we can calculate the total number of atoms in the cloud [4]. The optical density is related to the absorption we see in an absorption image and can thus be extracted from such images by fitting the absorption profile. For the example in figure 2.2 we find a total number of atoms $N = 0.96 \cdot 10^9$, which is also typical. The results show that we have been able to reproduce with metastable Ne the typical conditions for alkali atom BEC experiments [1], which is a first requirement for the *Gemini* project to succeed.

2.3 Optical molasses

Theory

When atoms are placed in a beam of light resonant with an atomic transition, the atoms will absorb photons. A photon carries a momentum $\hbar\vec{k}$ (k the wavenumber) and this momentum is transferred to the atom when it absorbs the photon. When many absorbtion cycles occur (assume the light stays resonant) the expectation value for the acquired momentum of the atom returning

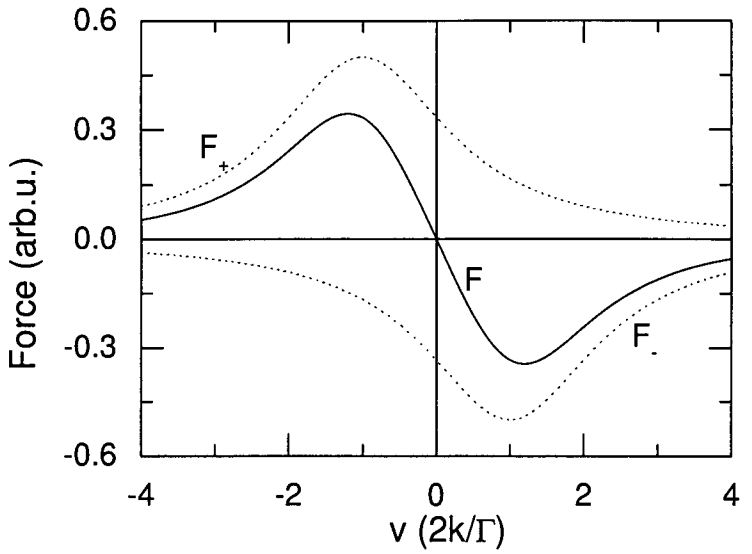

Figure 2.6: Force experienced by an atom moving with velocity v in the direction field of two red-detuned counterpropagating laser beams. The detuning is $\delta = -\Gamma/2$ and the intensity is $s_0 = 1$. The dashed curves represent the force according to equation 2.2 moving in the indicated $\pm$ direction. The solid curve is the total force experienced.

back to the ground state via spontaneous emission is zero, because of symmetry. However there is a net gain of momentum due to the *absorption* of photons. The total force which the light beam exerts on the atom is [8]

$$F = \hbar k \frac{\Gamma}{2} \frac{s_0}{1 + s_0 + (2\delta/\Gamma)^2}, \tag{2.2}$$

with Γ the natural linewidth of the transition, $s_0 = I/I_0$ the on-resonance saturation parameter in which I is the intensity of the light and I_0 the on-resonance saturation intensity, and $\delta = \omega_L - \omega_a$ the detuning in which ω_L is the laser frequency and ω_a the atomic transition frequency. If the atom has a velocity $\vec{v}$, ω_L has to be replaced by $\omega'_L = \omega_L - \vec{k} \cdot \vec{v}$ to account for a Doppler shift.

If we now picture an atom moving along the x-axis and we introduce two counterpropagating red-detuned laser beams, the atom will experience a velocity dependent force as depicted in figure 2.6. Its kinetic energy is reduced due to the successive absorption of counterpropagating photons. A lower limit for the achievable temperature by this method of cooling is [8] $k_B T_D = \hbar\Gamma/2$ (T_D the Doppler temperature), for a detuning of $\delta = -\Gamma/2$. The Doppler temperature for Ne* is $T_D = 196\mu$K.

If the two counterpropagating laser beams have opposite circular polarization, we obtain polarization gradients within the atomic cloud and another cooling mechanism occurs, that reduces the lower limit towards the recoil temperature. This is the temperature corresponding to the energy of one photon. For Ne* this limit is $T_R = (\hbar k)^2/(2m) \approx 2\mu$K.

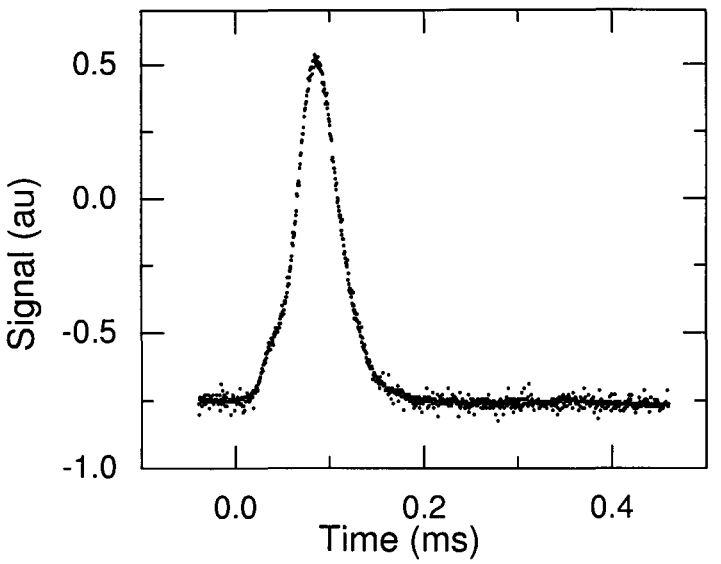

Figure 2.7: Signal registered by the channeltron above an atomic cloud in optical molasses, which starts at t=0.

Polarization gradient cooling occurs for velocities much smaller than those involved in Doppler-cooling. Also in the σ^+, σ^- case, the cooling force arises from an unbalanced absorption of photons from both beams. While this unbalance in Doppler-cooling arises from the Doppler shift, in polarization gradient cooling it arises from the velocity dependence of the distribution over Zeeman sublevels (i.e. among the different m_j) [9]. In the presence of a magnetic field, $\sigma^+\sigma^-$ cooling does not take place: the Larmor frequency must be small so as not to disturb the distribution between the different m_j due to the optical fields. This requires the magnetic field to be zero typically within several mG.

Experimental

To make the initial conditions for the start of evaporative cooling more favorable, we have tried to create an optical molasses in the $\sigma^+\sigma^-$ configuration. We have tried to accomplish this as follows.

First we load a MOT long enough to reach a steady state. Once the steady state has been reached we stop the loading by turning off the slow Ne* beam. After a delay, we turn off the MOT light followed by turning off the magnetic fields. After the MOT magnetic fields have completely decayed (which takes a finite time of ~1ms) the six trapping beams are turned on again for a few milliseconds creating the desired $\sigma^+\sigma^-$ configuration of light beams. For a direct indication of the temperature we observe the signal detected by a channeltron (see figure 2.1), which registers metastable atoms and is situated 4cm above the trapped cloud. The observed signal has the profile shown in figure 2.7.

When the cloud shows cooling, the maximum of the curve in figure 2.7 should shift to larger times, because the atomic velocities are smaller. We set

the 'compensation' coils to compensate for the earth magnetic field, creating $B = 0$ at the position of the cloud. The intensity and detuning of the $\sigma^+\sigma^-$ beams are varied as is the duration of the molasses. The parameter-space is scanned to maximize the time between the signal peak at the channeltron and the start of the molasses (largest peak delay). The largest observed delay was 90ms. According to an analysis of the signals [4] this should correspond to a temperature of approximately 40μK. When trying to measure the corresponding temperature by means of absorption imaging, however, the atom cloud as a whole was seen to be pushed away from the center of the trap in subsequent images, while no slower expansion than without the molasses phase was observed which should clearly have occured if the temperature was 40μK. This averaged velocity probably affected the indirect temperature measurement by means of the channeltron, leaving the channeltron peak-signal as an incorrect measure for the temperature.

The velocity gained seemed to stem from an unbalance in intensity between the σ^+ and the σ^- beam, caused be the fact that we use 'retro-reflected' beams. This means that a σ^+ beam, after passing the trapping chamber, is reflected and used as the σ^- beam (also passing a $\lambda/4$-plate twice). The result is that the final σ^- beam perceived by the cloud has passed a vacuum window, with a bad coating (85% transmission on double-pass), two times more than the perceived σ^+ beam did. The unbalance can be eliminated by using six separate beams instead of 'retro-reflected' beams, but the setup lacks the laser power necessary for this solution. Using the compensation fields it is also possible to correct for this unbalance by setting $B \neq 0$ but at the cost of sub-Doppler cooling, leaving the Doppler temperature as the lowest achievable temperature in this configuration.

The experiments on optical molasses were done at the time we also finished a new trapping chamber which should (and did) improve the bad vacuum of the trapping chamber in use at that moment. This new trapping chamber would also have vacuum windows with a better coating (measured transmission T=99.9% on double-pass). There was a combination of two facts that made us abandon the molasses-project: 1) the new trapping chamber was finished and could replace the old chamber. Rebuilding and characterizing the new setup cost a lot of time; 2) Two groups in Paris realized Bose condensation with metastables very recently, stimulating us to drop all projects not directly essential for achieving a BEC and pursue condensation within short time too[1]. While optical molasses helps to provide convenient initial conditions for evaporative cooling, it may not be essential.

At the moment the new trapping chamber is installed and the setup is completely operational again. The limitation of bad window coatings is not present anymore and therefore optical molasses might well be possible in the new trapping chamber, but up to now the molasses-project is put to rest until proven necessary for the realization of BEC.

[1] Actually this is also the advise both Paris groups gave us.

2.4 Magnetic trap (MT)

Theory

In a MOT, atoms can be trapped without restriction on the specific ground state level, i.e. on the projection of the angular momentum on the quantization axis. Magnetic trapping is based on the magnetic field dependence of the total atom energy. Since it is not possible to create a maximum in the magnetic field in free space [1], here we can only trap atoms whose energy minimizes with lowering magnetic fields. From equation (2.1) we know that these are the states with $m_j > 0$. We can make a magnetic field minimum with the cloverleaf trap of our setup [6]. Typical trapping frequencies are 46 and 350Hz in the axial and radial direction respectively.

The total number of trapped atoms in a MT will decay over time due to a finite lifetime of the metastable state, collisions with atoms from the background gas, and Penning ionization. Penning ionization is a binary collisional process in which one atom ionizes and the other atom returns to its groundstate,

$$\mathrm{Ne}^* + \mathrm{Ne}^* \rightarrow \mathrm{Ne} + \mathrm{Ne}^+ + e^- \tag{2.3}$$

in which the particles on the right have a (relatively) high temperature (T_{Ne}, T_{Ne^+} are of order $\mathcal{O}(10^2\mathrm{K})$ [10]). Apart from the loss due to an untrappable end state, Penning ionization leads to undesired heating effects. This process might be suppressed up to 4 orders of magnitude by spin polarizing the atoms [11]. In this case we have on the left of equation (2.3) a total spin S=2, while only S=0,1 can be formed by the end products, prohibiting the reaction.

We can write down a differential equation for the time evolution of the number of atoms in a MT,

$$\dot{N}(t) = -\frac{N(t)}{\tau} - \beta \int n^2(\vec{r}, t)\mathrm{d}^3 r, \tag{2.4}$$

with τ a time constant which accounts for the finite lifetime of the metastable state and background collisions, n the density of the cloud, and β the two-body collisional loss rate. By defining an effective volume $V_{eff} \cdot \int n^2 \mathrm{d}^3 r = N^2$ equation (2.4) can be rewritten to

$$\dot{N} = -\frac{N}{\tau} - \beta \frac{N^2}{V_{eff}}. \tag{2.5}$$

By measuring $\dot{N}$ as a function of N we can determine β by fitting if we know V_{eff}.

Experimental

To determine $\dot{N}$ we do an experiment that consists of two almost identical parts. We start a cycle by filling a MOT with atoms and wait until a steady state is reached. Then we stop the loading of the MOT by turning off the slow Ne* beam, switch of the light and successively also the MOT magnetic fields. Then a spin polarization light pulse is applied (in a weak magnetic field), after which the MT magnetic fields are switched on. The spin polarization pulse is a σ^+ beam which drives the atoms to the $m_j = +2$ state, thereby not only reducing Penning ionization but also increasing the number of trappable atoms. After

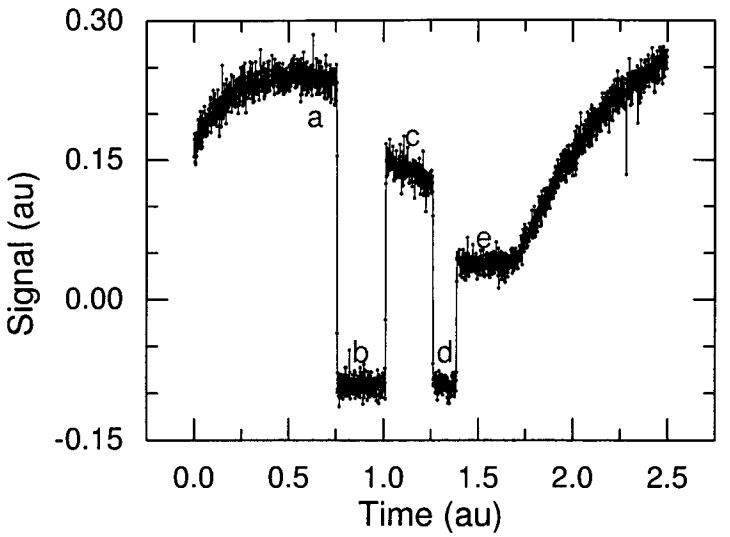

Figure 2.8: Fluorescence signal versus time during a cycle. The area labelled a is the last part of the loading of the MOT. Area b is the time the magnetic trap is on. Recapture in the MOT can be seen in the area c followed by d which is the time used to let the atoms move out of the area. Area e is the background signal (trapping lasers on) immediately followed by again a loading of the MOT.

the spin-polarization pulse the MT is switched on and the cloud is compressed in 1s by increasing the trapping frequency[2].

Up to here both parts of the experiments are equal. The only difference between both parts is that at this point a storage period of 0.5s is inserted in one part and omitted in the other. Both parts then continue in the same way again.

After the optional holding time in the magnetic trap, its magnetic fields are turned off. The remaining atoms are now recaptured in a MOT, by turning on the magnetic fields of the MOT again and then the trapping beams. After a short delay the magnetic fields and lights of the MOT are turned off again and after another delay (allowing atoms to leave the trapping center) turned back on for a background measurement, ending the cycle.

During a cycle the fluorescence is recorded on a oscilloscope which is read out by a computer, see figure 2.8. The computer registers the fluorescence signal of: a) the steady state MOT; c) the recaptured MOT; e) the background signal. Part I and II of the experiment are repeated often in an automated loop for statistics. This experiment is repeated for various values of initial number of atoms (i.e. in the steady state MOT). Variation of the number of atoms is realized by lowering the output of the slow atomic beam.

Part I and part II of the same experiment are taken together. Part I yields a relation between the number of atoms in the MOT (N_0) and the number of

[2]If we would not increase the trapping frequency but just hold the atoms for a short time (~100ms) in the MT and then release them from the MT and back into the MOT, we can deduce the MOT to MT transfer efficiency from a fluorescence trace.

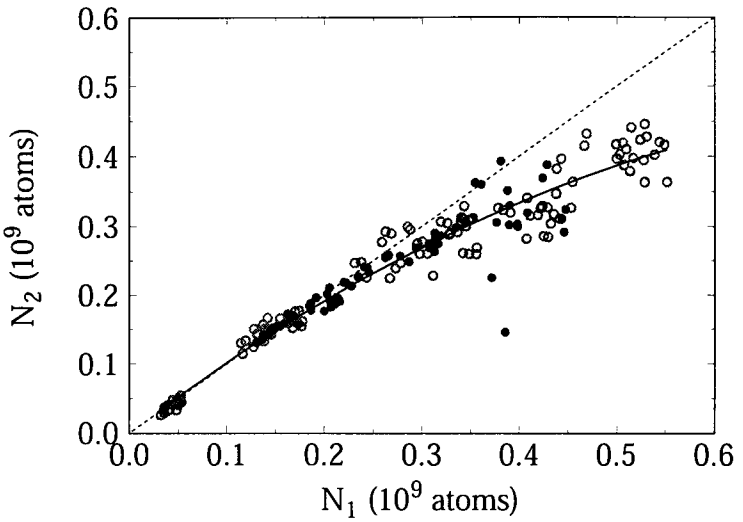

Figure 2.9: Graph of the total number of atoms in the compressed MT after a time Δt=0.5s, N_2, versus the number of atoms initially in the MT, N_1. From this data a value for $\beta_{pol} = 8 \cdot 10^{-11}$ can be determined. Both isotopes seem to yield the same β_{pol}. The open dots refer to ^{20}Ne measurements, whereas the solid dots refer to ^{22}Ne.

atoms in the MT right after the compression, which we denote by N_1. Part II yields a relation between N_0 and the number of atoms remaining after the cloud has spend a time Δt=0.5s in the MT, which we will denote by N_2. From the experiment (differing only in initial number of atoms) we thus obtain a relationship between N_1 and N_2, which are plotted in figure 2.9. Fitting $N_2 = -a \cdot N_1 - b \cdot N_1^2$ to this curve yields the value for $\beta = \frac{bV_{eff}}{\Delta t}$. We determine V_{eff} from its relation with the temperature and the known shape of the trap [6]. Starting with a MOT of $T = 600\mu$K the temperature in the compressed MT will be $T = 1.0$mK. With typically $N = 10^9$ particles we find a central density of $n_0 = 6 \cdot 10^{10}$cm^{-3} and an effective volume V_{eff}=0.079cm^3. Using these values we find a spin-polarized two-body decay rate $\beta_{pol} = 8 \cdot 10^{-11}$cm^{-3}/s from the data in figure 2.9.

This value for β_{pol} is quite large, since it would imply that an atomic cloud of density $8 \cdot 10^{11}$ would have a lifetime τ=1s. This density has to be compared with a density of the order $10^{13} \sim 10^{14}$cm^{-3} in a condensate [10] at which point the lifetime would be less than 1ms. This would be prohibitive for our chances to create a Ne* BEC.

The result of this measurement may be masked by other effects. A possible effect which would yield too large a β_{pol} is spontaneous evaporative cooling. This effect can be imagined as follows. Assume a Maxwell-Boltzmann distribution (MB) for the trapped atoms. Atoms constituting the tail of this distribution have an energy larger than the depth of the trap and will therefore escape from the trap. The tail from the MB distribution is thus emptied, but due to collisions in the atomic cloud the tail is refilled. These 'new' high-energy atoms will also

escape from the trap. This means an additional loss of the total number of atoms in the trap. The more efficiently the emptied MB tail is refilled, the more atoms will be lost from the trap. Since this rethermalization occurs via elastic scattering, which occurs at a rate $n\sigma v$ (n the density, $\sigma = 8\pi a^2$, a the scattering length, and v the velocity), we expect greater losses for larger densities (as we observe in figure 2.9) and also for larger scattering lengths. The losses in the measurement can therefore also be explained by a combination of however a sufficiently large value of a, accounting for the spontaneous evaporative cooling, as well as a large value for β, accounting for two body collisional losses. A larger $|a|$ must imply a smaller β and vise versa. Setting $a = 0$ consequently yields an upper limit for β. Since setting $a = 0$ equals exclusion the spontaneous evaporation effect, the beta found above ($\beta_{pol} = 8 \cdot 10^{-11}\mathrm{cm}^3/\mathrm{s}$) is an upper limit. Setting $\beta = 0$ requires a rather large value $|a| \approx 400\mathrm{a}_0$ to explain our observations. This would be a very desirable situation since we would loose no atoms due to two-body collisions and have a very effective rethermalization. This situation would be favorable for our changes to create a Ne* BEC.

2.5 Current and future experiments

Currently our group works on rethermalization experiments which have to pinpoint the value for the scattering length. A better knowledge of the scattering length gives more insight in the feasibility of a metastable Ne BEC. Signs of rethermalization, which is of great importance during evaporative cooling, are believed to be seen.

The next step will be experiments with evaporative cooling which ultimately has to increase the phase-space density to 2.61. If the scattering length for ^{20}Ne* collisions turns out to be largely negative, this would prohibit realization of a BEC with this isotope [1]. However a negative scattering length for ^{20}Ne* collisions does not imply a to be negative for ^{22}Ne* collisions too. This means that the possibility for a ^{22}Ne* BEC is not excluded in advance in this case. Since we are at the final stage on the road to BEC and we can trap both isotopes with our experimental setup, the prospects for making a Ne* BEC in the near future with either one or both isotopes are quite promising.

2.6 Conclusions

In the experimental group an absorption imaging system was set up and tested. The tests of the absorption imaging system yielded values for the total number of atoms in a MOT ($N \approx 10^9$). The system was also used to determine temperatures of atoms in a MOT by observing the time dependence of the atomic cloud expansion on release. Temperatures around T=1mK were found, which in combination with the total number of atoms are values comparable to those in alkali BEC experiments.

To decrease the temperature of the atoms when transferred from a MOT to a MT, we have tried to implement a $\sigma^+\sigma^-$ optical molasses stage. We were not able to observe a decrease in temperature, probably due to an intensity unbalance of the σ^+ and σ^- beam, arising from bad window coatings in combination with the use of 'retro-reflected' beams. The setup has been changed and the

problem of bad window coatings is solved, but a change of priorities put the subject 'optical molasses' to rest.

Without an intermediate stage of optical molasses the atoms are transferred to a MT and the loss rate from this MT has been measured for atoms in a spin-polarized state. From the obtained data we can deduce limits for the two-body loss rate β_{pol} and the scattering length a. Setting a=0 we find an upper limit to the two-body loss rate $\beta_{pol} = 8 \cdot 10^{-11}\mathrm{cm}^3/\mathrm{s}$; a combination which would prevent us from obtaining BEC, by too short a lifetime of the atomic sample and lack of rethermalization. By setting β=0 the same data can be explained with a scattering length $a \approx 400\mathrm{a}_0$; in this case the sample would not decay due to two-body collisions and the scattering length is large (comparison: $a \approx 100\mathrm{a}_0$ for ^{87}Rb), which are good conditions to obtain BEC.

Part II

Analysis of the Rb singlet and triplet ground-state potentials

Introduction

In this part of the thesis we will focus on the analysis of interacting cold rubidium atoms. In the group of prof. Verhaar, we have performed such an analysis. We have submitted this work as a Phys. Rev. Letter, which has in the meantime been accepted for publication. This paper has been included in this report as chaptere 4. Since Phys. Rev. Letters have to meet certain criteria, chapter 4 is short on some details. In chapter 3 some aspects concerning the analysis are described more extensively, starting in the first two sections with a description of the interactions which we include in the calculations. Section 3.3 shows how the potential we use is constructed. Section 3.4 deals with the accumulated phase method and shows how we relate the properties of the different isotopes to each other. Section 3.5 contains some aspects of scattering theory like the concept of scattering length, and is followed by a brief introduction to coupled channels calculations. In section 3.7 the physical background behind Feshbach and shape resonances is discussed, while the chapter is concluded with a description of the numerical procedure of the fitting process in section 3.8.

Chapter 3

Interactions of ultracold alkali atoms

3.1 One particle Hamiltonian

The atoms in group one of the periodic table make up the group of alkali atoms. All these atoms have one electron in an outer s-shell which will be called valence electron throughout the remaining part of this chapter. This electron has spin $s=\frac{1}{2}$ while the nucleus has spin i which equals $\frac{5}{2}$ for ^{85}Rb and $\frac{3}{2}$ for ^{87}Rb. These spins combine to a total angular momentum of $\vec{f} = \vec{s} + \vec{i}$ with each $\vec{f}$-state $(2f + 1)$-fold degenerate. In total there are $2(2i + 1)$ possible 'ground states' for an alkali atom, split over two different f-states. Note that lower case characters are used to indicate single atom properties while we reserve capitals for two-atom systems.

The above mentioned degeneracy for alkali atoms is lifted by interactions both within the atom and with external fields. The nuclear spin interacts with the electron spin, leading to the hyperfine splitting for an atom j,

$$V_j^{hf} = \frac{a^{hf}}{\hbar^2} \vec{s}_j \cdot \vec{i}_j \tag{3.1}$$

with a^{hf} the hyperfine constant.

This atom j placed in a magnetic field $\vec{B}$ experiences a Zeeman energy

$$V_j^Z = \left(\gamma_{e,j}\vec{s}_j - \gamma_{n,j}\vec{i}_j\right) \cdot \vec{B}, \tag{3.2}$$

where $\gamma_{e,j}$ and $\gamma_{n,j}$ are the electronic and nuclear gyromagnetic ratios. The behavior of the valence electron in alkali atoms is influenced by the electrons filling the inner shells causing γ_e to be slightly different from 2. While s and i have the same order of magnitude, the ratio γ_e/γ_n is of order 10^3.

Equations (3.1) and (3.2) lead to the familiar graphs for the energy of the hyperfine states as a function of the magnetic field $B\hat{z}$ as depicted in figure 3.1. We will label these one atom hyperfine states by $|f, m_f\rangle$ even though f is only a good quantum number for $B = 0$.

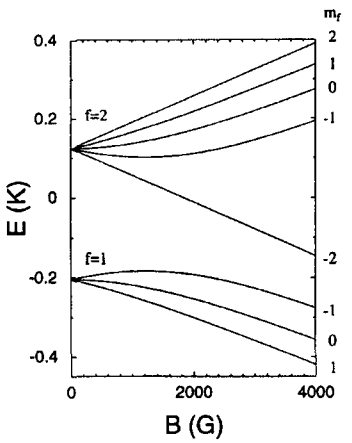

Figure 3.1: Energy of the hyperfine states of ^{8}7Rb as function of the magnetic field strength B. Quantum numbers identifying the different configurations at $B = \infty$ are indicated.

3.2 Two particle Hamiltonian

Due to the difference in mass of an electron and a nucleus the time scale for electronic processes is very short compared to the time scale of collisions. During a collision it is therefore possible for electrons to adiabatically adapt themselves to the nuclear motion, allowing one to separate the Schrödinger equation in an electronic and a nuclear part. Such a separation is called the Born-Oppenheimer approximation. In this approximation it is possible to solve the electronic equation for fixed positions of the nuclei and subsequently use the energy eigenvalue V^C of this solution to calculate the nuclear motion. The resulting central interaction V^C represents all Coulombic interactions between the electrons and nuclei of both atoms.

In a binary collision of alkali atoms there are two possibilities for the total electron spin. Since each atom has one valence electron $s_1 = s_2 = \frac{1}{2}$, the resulting total spin can be $S = 0$ or $S = 1$ corresponding to the singlet and triplet configuration. The central interaction can be written

$$V^C = V_S(r)P_S + V_T(r)P_T, \tag{3.3}$$

with $P_{S,T}$ the projection operators on the singlet and triplet subspaces and r the interatomic separation.

The fermionic character of electrons requires the total electron wavefunction to be antisymmetric. The antisymmetric singlet state must therefore be combined with a symmetric spatial wavefunction and the triplet configuration combines with an antisymmetric spatial wavefunction. In the triplet case there is a vanishing probability of the electrons being between the nuclei. A triplet configuration therefore has a higher internal energy (larger repulsion between the nuclei) causing the corresponding interaction potential to be more shallow compared to the singlet configuration. These potentials, differing by twice the

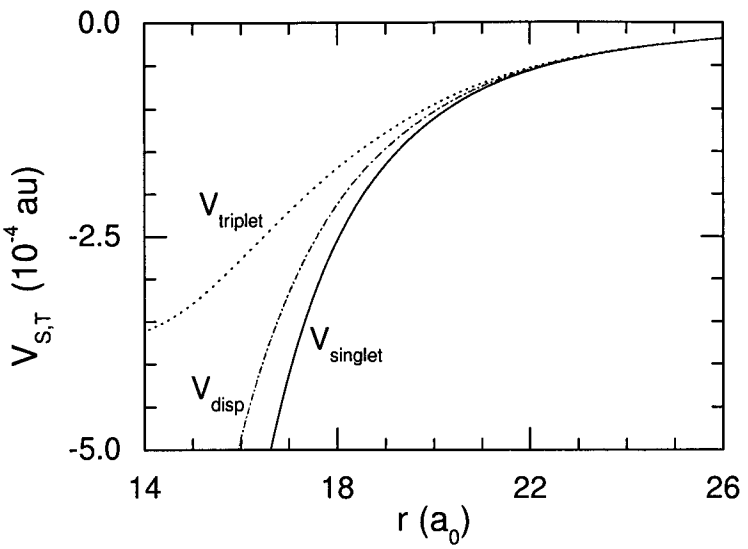

Figure 3.2: Singlet and triplet groundstate potentials for Rb according to eq. (3.4). V_{disp} is also depicted.

exchange energy V_{exch}, can be written as

$$V_{S,T} = V_{disp} - (-1)^S \; V_{exch}, \tag{3.4}$$

with

$$V_{disp} = \frac{-C_6}{r^6} + \frac{-C_8}{r^8} + \frac{-C_{10}}{r^{10}} + \frac{-C_{11}}{r^{11}} + \frac{-C_{12}}{r^{12}} + \ldots, \tag{3.5}$$

in which C_n are dispersion coefficients with C_6 representing the electric dipole-dipole interaction. Higher coefficients with even n represent second-order contributions of higher multipoles. The term C_{11} arises in third order and is negative (*i.e.* repulsive). Except for the extended analysis described in section 4.4, only the first three terms of eq. (3.5) are taken into account.

For Rb, C_6 has been determined both completely theoretically and from experiments. Higher-order coefficients C_8, C_{10}, and C_{12} for Rb are until now only available from completely theoretical determinations (see *e.g.* refs. [12, 13]). The singlet and triplet potentials for Rb interactions are shown in figure 3.2 and the relative importance of the contributing terms are depicted in figure 3.3.

An analytic expression for the asymptotic exchange energy in eq. (3.4) has been derived by Smirnov and Chybisov [14] and found to be

$$V_{exch} = J r^{\frac{7}{2\alpha}-1} e^{-2\alpha r}. \tag{3.6}$$

In eq. (3.6), $-\alpha^2/2$ is the atomic ionization energy and J is a normalization constant; r and α in atomic units (see table A.3). It is difficult to calculate J from first principles, because it is proportional to the fourth power of the normalization constant of the valence-electron wavefunction [14], which is difficult to calculate.

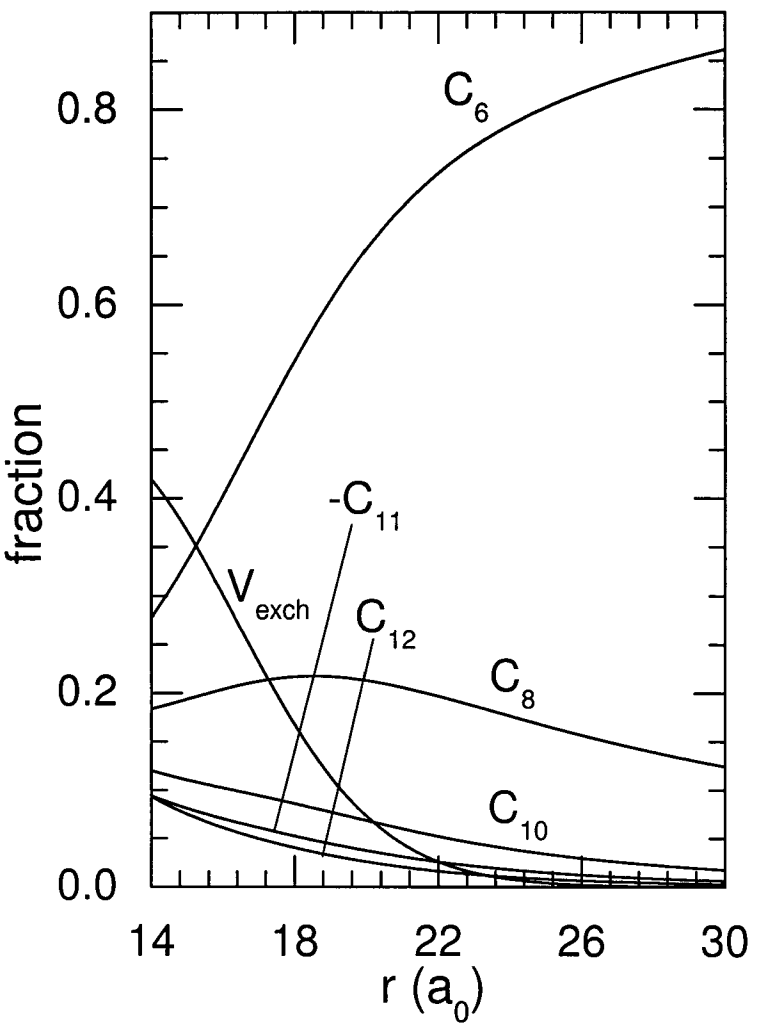

Figure 3.3: Relative partial contribution of indicated terms to the total singlet potential V_S (eq.(3.4)). The fraction is defined to be V_{term}/V_S. For the C_{11} contribution, which is negative, the absolute value is shown to illustrate the 'competition' with a C_{12} contribution. Parameters resulting from our analysis as described in chapter 4 are used. These parameters are summarized in table 4.1.

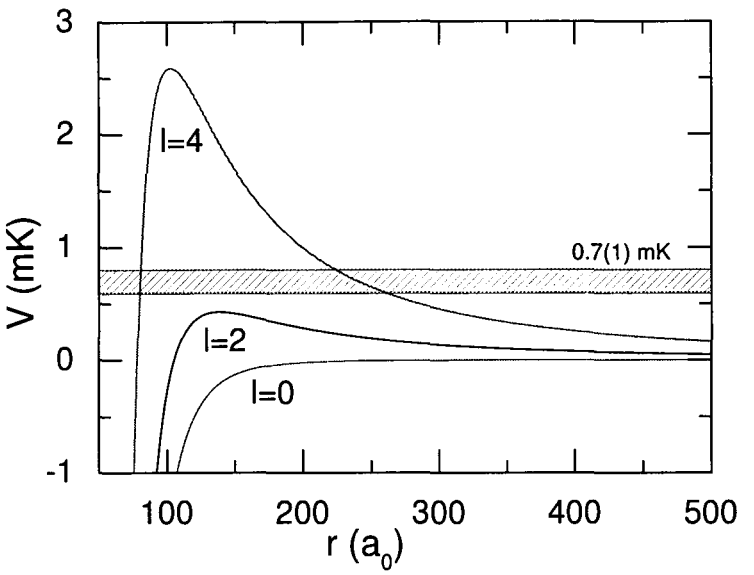

Figure 3.4: Centrifugal barrier for ^{85}Rb. The stroked bar indicates the position of a measured l=4 shape resonance used in our fit. The exchange energy (3.6) is negligible leading to the same potential for singlet and triplet at the interatomic separations regarded.

The total Hamiltonian for two colliding ground-state alkali atoms becomes

$$H = \frac{\vec{p}^2}{2\mu} + \sum_{j=1}^{2} \left(V_j^{hf} + V_j^Z \right) + V^C, \tag{3.7}$$

in which the first term represents the kinetic energy with μ the reduced mass of the atoms and $\vec{p}$ the momentum operator. In the l, m_l representation this term has the form

$$\frac{\vec{p}^{\,2}}{2\mu} = -\frac{\hbar^2}{2\mu} \left(\frac{\partial^2}{\partial r^2} - \frac{l\,(l+1)}{r^2} \right). \tag{3.8}$$

The last term is a centrifugal barrier arising from the rotation of the molecule (see figure 3.4). The Zeeman term is straightforward.

For collisions of two identical atoms the hyperfine term can be written as the sum of two parts each having different symmetry with respect to the exchange of electron or nuclear spin,

$$V^{hf} = \frac{a_{hf}}{2\hbar^2}(\vec{s}_1 + \vec{s}_2) \cdot (\vec{i}_1 + \vec{i}_2) + \frac{a_{hf}}{2\hbar^2}(\vec{s}_1 - \vec{s}_2) \cdot (\vec{i}_1 - \vec{i}_2) \equiv V^{hf+} + V^{hf-}. \tag{3.9}$$

The convenience of this splitting arises from the fact that V^{hf-} is the only term coupling singlet and triplet states [15].

For the interactions mentioned up to now the system of two colliding atoms is invariant under independent rotations of the spin system and of the orbital system around the axis through the overall center of mass parallel to the magnetic

field. Therefore the projection of the total spin angular momentum $\vec{f}_1 + \vec{f}_2 \equiv \vec{F}$ and of the orbital angular momentum $\vec{l}$ along this axis are separately conserved during the collision. Since V^C only depends on r and not on $\hat{r} = \vec{r}/r$ $\vec{l}$ is even conserved as a 3D vector. As a consequence, m_F and the rotational quantum numbers l and m_l are good quantum numbers.

Two other interactions are present which are much smaller than the above mentioned effects. The first one is a direct interaction between the spins of the electrons via their magnetic moment. This very weak interaction is given by

$$V^{\mu}(\vec{r}) = \mu_0 \frac{\vec{\mu}_1 \cdot \vec{\mu}_2 - 3(\vec{\mu}_1 \cdot \hat{r})(\vec{\mu}_2 \cdot \hat{r})}{4\pi r^3}, \tag{3.10}$$

with $\vec{\mu}_j$ the electron magnetic dipole moment of atom j. We leave out the much weaker magnetic dipole interactions in which the nuclear magnetic moments are involved. Second, the spin-orbit interaction V_{SO} of the spins of the valence electrons is given by a complicated expression [16] that contains contributions from the magnetic fields generated by the orbital currents of electrons and nuclei. For interatomic distances larger than 13 to 14 a_0 this complicated expression reduces for one valence electron outside closed shells in both alkali atoms to the well-known sum of two atomic spin-orbit couplings:

$$V^{fs} = \sum_{j=1}^{2} \frac{2E^{fs}}{3\hbar^2} \vec{\ell}_j \cdot \vec{s}_j, \tag{3.11}$$

with $\vec{\ell}_j$ the electronic angular momentum of atom j, and E^{fs} the fine-structure splitting.

Separate ground state alkali atoms ($^2S_{1/2}$) have an electronic angular momentum $l = 0$ and therefore contributions of (3.11) vanish in this case. However, for small interatomic separations the electron clouds overlap and an important additional contribution arises as a second order effect in V_{SO} via an intermediate coupling to electronically excited molecular states [17]. Now, V_{SO} has the form of a sum of terms for the two valence electrons,

$$V_{SO} = \sum_{i=1}^{2} \vec{b}_i \cdot \vec{s}_i, \tag{3.12}$$

where $\vec{b}_i$ is an orbital pseudovector like $\vec{s}_i$ (a normal vector under rotations but even under space inversion, instead of odd as for an ordinary vector). One can show by means of symmetry considerations that the only effect of V_{SO} in our case is a splitting of the $\Omega = |m_{Sz}| = 0$ and 1 substates in the triplet subspace of Hilbert space. The triplet potential curve $a^3\Sigma_u^+$ thus splits up into two curves $V_{\Omega=1}(r)$ and $V_{\Omega=0}(r)$. This splitting is similar to that induced by the magnetic dipole spin-spin interaction (3.10) between the valence electron spins whose only effect is also an Ω splitting.

In total, we thus have a spin-spin interaction V^{ss} between the valence electrons, consisting of two parts:

$$V^{ss} = (V^{ss})^{\mu} + (V^{ss})^{so}, \tag{3.13}$$

a magnetic dipole part and a part arising from V_{SO} in second order. The dipole part, when expressed in the spin vectors $\vec{s}_i$ is given by

$$(V^{ss})^{\mu} = \frac{\mu_0 \gamma_e^2}{4\pi r^3} \left[\vec{s}_1 \cdot \vec{s}_2 - 3(\vec{s}_1 \cdot \hat{r})(\vec{s}_2 \cdot \hat{r})\right]. \tag{3.14}$$

The part $(V^{ss})^{so}$ has effectively the same spin-angle structure (the factor between square brackets), but multiplied by a different radial factor. This factor has an exponentially decaying form for increasing r and has been calculated via an *ab initio* electronic structure calculation by Mies et al. [18].

The total V^{ss} apparently has the structure of a scalar product of two irreducible spherical tensors of rank 2:

$$V^{ss} = f(r)\,[(\vec{s}_1, \vec{s}_2)_2 \cdot (\hat{r}, \hat{r})_2]\,. \tag{3.15}$$

As a consequence, it is invariant under the simultaneous 3D rotations of the internuclear vector $\vec{r}$ and the spin degrees of freedom, thus conserving the total molecular angular momentum. On the other hand, it is not invariant under independent rotations of $\vec{r}$ and the spin degrees of freedom. It therefore obeys triangle type S and l selection rules for a second rank tensor: it couples only spin triplet states and it couples for instance the $l = 0$ and 2 rotational states of the molecule.

As mentioned before, the spin-spin interaction is rather weak and are therefore expected to influence the final results of our calculations only mildly. As these interactions do not conserve l, m_l and therefore introduce many states that have to be included in the calculations, slowing them down enormously, we leave out these interactions in the major part of the analysis described in chapter 4. That these interactions cannot always be neglected is illustrated by the predicted (mixed channel) Feshbach resonance in chapter 4 which arises from a coupling between an $l = 0$ and an $l = 2$ state.

3.3 Constructing a potential

As explained in section 3.2 two interaction potentials suffice for the description of two interacting alkali atoms: a singlet and a triplet potential, see figure 3.2. When calculating the properties of two interacting Rb atoms we actually make use of the explicit expression for the potentials defined by eq. (3.4) only for large atomic separations ($r \gtrsim 22a_0$, in part of the analysis $r \gtrsim 16a_0$).

In this section the method for the construction of our potentials is described. Singlet and triplet potentials are treated separately because of the availability of a highly accurate inner part of the singlet potential. The singlet potential is treated first.

Singlet potential

Figure 3.3 shows that for small interatomic distances ($r \lesssim 22a_0$) dispersion terms beyond C_{10} become important. For small separations more and more terms become important, and an analytic expression for $V_{S,T}$ will contain increasingly more terms. In this range the interaction potentials can more accurately be obtained by *ab initio* calculations or by deriving a potential from experimental data. Krauss and Stevens have performed *ab initio* calculations for both $S = 0$ and $S = 1$ Rb potentials at small interatomic distances [19]. Seto *et al.* recently derived a singlet potential for Rb from 12148 measured transition frequencies (with uncertainties of 0.001 cm^{-1}) belonging to bound states having outer turning points up to $25a_0$. As in the latter work the potential is fit to the experimental data by matching differences between calculated bound

states to measured frequencies, only the shape of the potential is determined, still allowing a 'vertical' energy shift. Seto *et al.* used a 'modified Lennard-Jones oscillator' [20, 21] model for their fit. This type of model allowed them to incorporate a known asymptotic behavior in their fit, for which they used a sole C_6/r^6-term.

For small interatomic distances we will use the singlet potential derived by Seto *et al.* [22] because of its high accuracy. Since we use eq. (3.4) for the long-range potential, a switch between inner and outer potential must be made. A logical choice for the switching position would be to use the Seto-potential up to interatomic distances equal to the outer turning point of the highest bound state incorporated in Seto's fit. However a property of the MLJ model is the pre-determined asymptotic behavior at large separations. Since Seto *et al.* chose a sole C_6/r^6-term (C_6=4650a_0) for this pre-determined asymptotic behavior we may expect less good agreement with the (less simple) asymptotic behavior implied by eq. (3.4). According to Nikitin [23] the description of the interaction potentials in asymptotic form will be valid down to $\sim 13a_0$. This allows us to choose the switching position at interatomic separations larger than $\sim 13a_0$.

We want to use the Seto-potential to as large as possible separations, but are limited by the boundary condition Seto *et al.* imposed. In the range left of the onset of the boundary condition the Seto-potential is purely determined by the measured transition frequencies and must consequently obey a full expression of the asymptotic behavior which we approximate by eq. (3.4). Studying figure 3.3 we see an increasing contribution of dispersion terms beyond C_{10} with decreasing interatomic separation. This implies that we cannot choose the switching point at separations too small using only the first three dispersion terms of eq. (3.4). Choosing the switching point at a separation too small would lead to a mismatch between the Seto-potential (locally having the behavior determined by the transition frequencies) and our potential (which then does not contain all dispersion terms which are important at these small separations). Note that the contributions of the C_{11} and C_{12} term are almost equal in magnitude thereby roughly cancelling each other as they have opposite sign, making the latter restriction on the position of the switching point less strong. Figure 3.5 illustrates the ratio of the potentials defined by Seto *et al.* and equation (3.4) for the first three dispersion terms taken into account. The Seto-potential is 'vertically' adjusted to equal our asymptotic potential at $21.5a_0$. The values used for the dispersion coefficients are the resulting values from our analysis (column A, table 4.1). Vertical adjustment at a larger separation moves the curve slightly downwards but still shows a 'plateau' around $21.5a_0$. The existence of the plateau underlines the consistency of our approach.

We now construct the singlet potential by choosing the switching point r_S around $21.5a_0$. As switching function we use

$$f(r, r_S, w) = \frac{1}{2}\left[1 - \tanh\left(\frac{(r - r_S)}{w}\right)\right] \tag{3.16}$$

as illustrated in figure 3.6. At r_S the Seto-potential is 'vertically' adjusted to equal our asymptotic potential at $21.5a_0$. The singlet potential becomes[1]

$$V_{sing}(r) \quad = \quad f(r, r_S, w) \cdot V_{Seto}(r) +$$

[1]Note that V_{sing} is the constructed singlet potential valid for all interatomic separations and V_S is the singlet potential in the asymptotic form of equation (3.4)

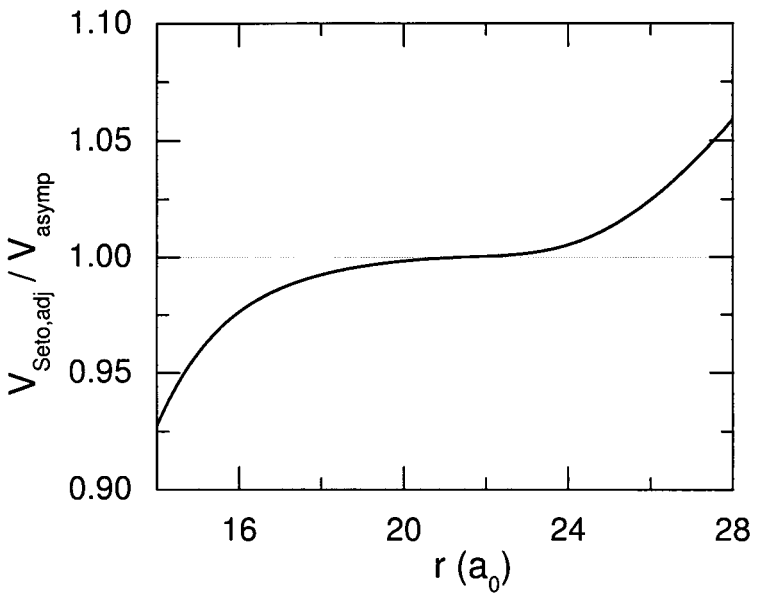

Figure 3.5: Ratio of the potentials constructed by Seto *et al.* and the potential according to equation (3.4) with only the first three dispersion terms taken into account. The Seto-potential is 'vertically' adjusted to equal our asymptotic potential at $21.5a_0$. The values used for the dispersion coefficients are the resulting values from our analysis (column A, table 4.1). Vertical adjustment at a larger separation moves the curve slightly downwards but still shows a 'plateau' around $21.5a_0$

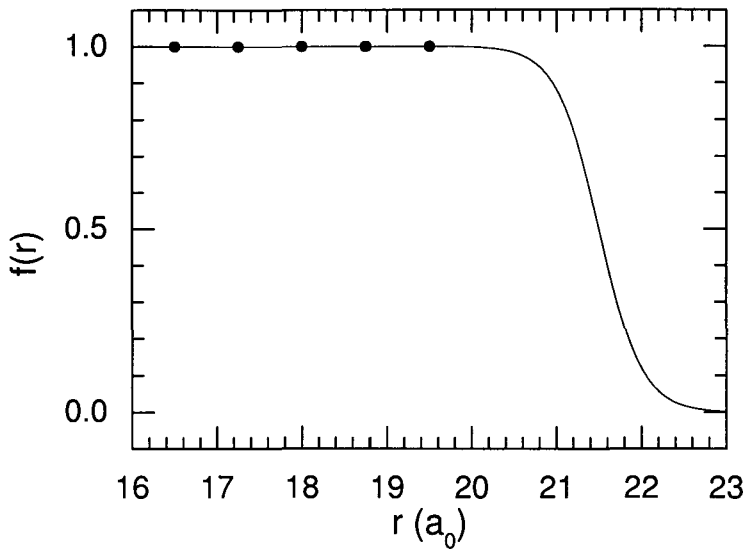

Figure 3.6: The switching function eq. (3.16). The values for r_S and w are $21.5a_0$ and $0.5a_0$ respectively. The dots represent the positions where we require $V_{Seto}/V_S = 1$ (see text).

$$[1 - f(r, r_S, w)] \cdot V_{eq.(3.4),S=0}(r). \tag{3.17}$$

Over a width $2w$, V_{sing} switches from the Seto-potential to the asymptotic potential. The optimal value for w is determined by varying w and plotting the resulting potential and its derivatives. For non-optimal values of w 'bumps' and 'dips' show up in the potential. It is checked that the potential and its derivatives look smooth. Choices for r_S and w are made within the boundary condition that the highest bound states which were used by Seto *et al.* (outer-turning point $\sim 25a_0$) are correctly predicted by the newly constructed potential. This led to the choices $r_S = 21.5a_0$ and $w = 0.5a_0$. These values for r_S and w can be used for the entire domain of parameter space we are interested in. This domain is spanned by the most recent values for C_6, C_8, and J with their uncertainties. Variations to w on the order of 0.3 have no significant effect. The switching point r_S may be chosen in the interval $21a_0 < r_S < 23.5a_0$ without significantly changing the final results.

In our paper we also carry out an extended analysis in which we assume the expression (3.4), including C_{11} and C_{12} terms, to be valid in an even larger interval extending to r values left of $21.5a_0$. Comparing the (3.4) singlet potential with the Seto potential opens a possibility to determine also C_{10} and C_{11}. Not exactly known is down to what separation eq. (3.6) will be a good approximation for the exchange potential as for smaller separations terms of higher order may gain importance. However, we believe that the asymptotic expression (eq. (3.4)) will be valid at least down to $16a_0$.

In section 4.4 we perform an analysis with such an extended asymptotic potential function. Taking C_{12} from the literature [13] we determine values for the coefficients C_{10} and C_{11} as follows. At five values for the interatomic

separation r ($16.5a_0 < r < 19.5a_0$, see figure 3.6), the V_{Seto} values are treated as five additional 'experimental data' which we fit with the extended equation (3.4) assuming a standard deviation of 0.5%. The final values for the 8 fitted parameters do not significantly depend on the chosen value for the standard deviation. The lower boundary of the 'interval of comparison' can be shifted to $18a_0$ without significantly affecting the end results of the fit.

Triplet potential

Note that in the extended analysis we assume the Smirnov-Chibisov asymptotic form for V_{exch} (as well as the extended V_{disp}) to be applicable down to interatomic separations of $16a_0$. This implies that we can use V_{exch} to deduce the triplet potential between $16a_0$ and r_S from the accurate Seto singlet potential: we equate it to[2] $V_{sing} + 2V_{exch}$. Given the dispersion coefficients C_n and the parameter J we are now able to construct the singlet potential for all r and the triplet potential right of $16a_0$: see figure 3.7. Left of $16a_0$ the triplet potential is less well-known. As mentioned above Krauss and Stevens [19] performed an *ab initio* calculation of the singlet and triplet potentials, and a comparison of the singlet potential with the (vertically shifted) Seto singlet potential left of $16a_0$ shows rather large differences, suggesting a similar limited reliability of the *ab initio* triplet potential in the same interval. Therefore, we prefer to apply a model-independent approach in this interval: the accumulated phase method.

3.4 Accumulated phase method

The accumulated phase method is an approach that enables one to bypass the insufficiently known potential left of an interatomic distance r_0 by means of a boundary condition on the wave function at r_0. The idea is that the boundary condition contains less parameters (actually three) than the detailed potential left of r_0. The only conditions that need to be fulfilled for the method to be applicable are that 1) The total coupled-channel scattering or bound state problem at hand should reduce to a set of decoupled channels described by a radial Schrödinger equation, 2) locally, in a small environment of r_0 the WKB should be valid, enabling one to specify the boundary condition as a phase of the real-valued oscillating radial wave function, 3) the energy E and l values that play a significant role in the problem are in sufficiently small intervals that allow for a rapidly converging expansion of the WKB phase in powers of E and $l(l+1)$, thus containing a small number of parameters.

Our scattering and bound state problems are ideal for summarizing the history of the atom-atom motion left of a radius r_0 in terms of an accumulated phase, although condition 1) is much less easily fulfilled than in previous work of our group. An r_0 value of about $19a_0$ used to guarantee that the singlet and triplet potentials differed by many times the part V^{hf-} of the hyperfine interaction coupling the singlet and triplet states for $r < r_0$. The excessive accuracy that we have to require in the present work would in principle lead us to r_0 values even left of $16a_0$. We can, however, avoid that by a subtle extension of

[2] We use V_{sing} here instead of V_{Seto} to exploit the high accuracy of V_{Seto} left of r_S, keeping the triplet potential accurate right of r_S because of the switch to the asymptotic expression in V_{sing} for large r.

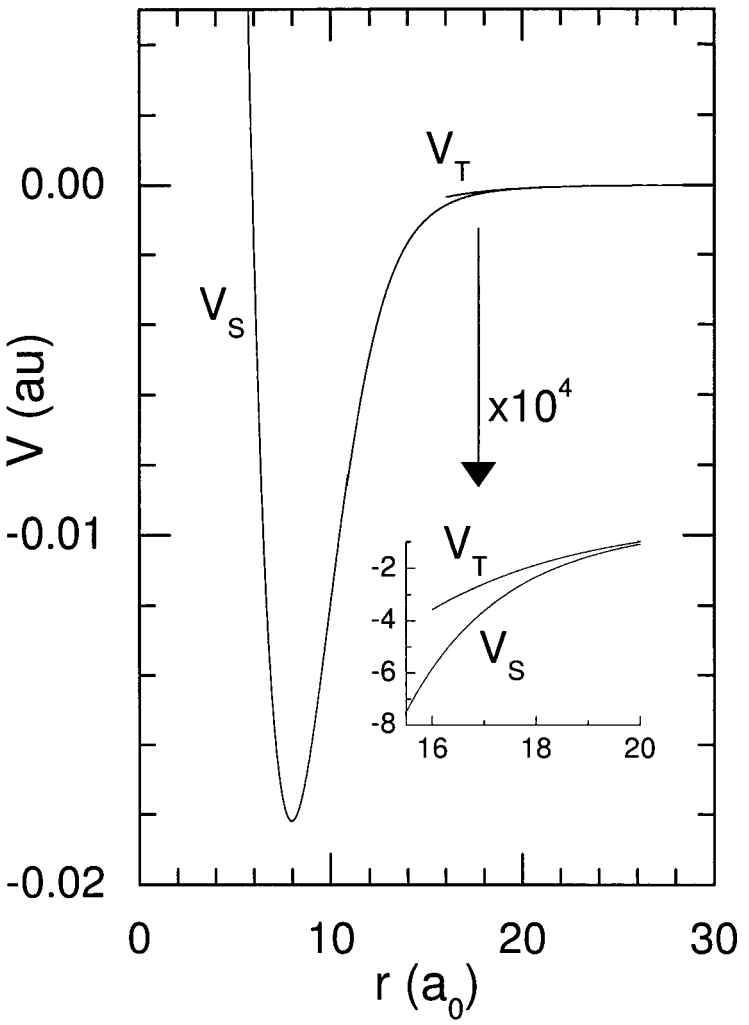

Figure 3.7: Singlet and triplet potentials for Rb.

the original accumulated phase method as we proposed it: do not neglect the influence of the V_{hf-} mixing completely. Take it into account in so far as it can be expressed in the pure singlet and triplet potentials in $r \geq r_0$.

To understand this, consider the coupled channel problem in the *adiabatic approximation*, i.e., the approximation in which the collision system evolves independently along the adiabatic potential curves found by diagonalizing the local total potential matrix in a socalled adiabatic basis of spin states [24]. Our calculations show that this approximation is valid up to interatomic separations a considerable distance larger than $16a_0$. Within this approximation V_{hf-} has two kinds of effects: it influences the adiabatic spin states and it influences the diagonal radial phases. Now, we neglect the latter so that we can work with pure singlet and triplet phases at r_0, but include the former as it depends only on (the difference of) the singlet and triplet potentials at r_0 and not at smaller radii.

With respect to conditions 2) and 3) above, we note that for the ultracold colliding atoms and near-dissociation bound states we are considering, E is very close to 0 ($< 1\mu$K) and l is at most 4. As a consequence, the influence of E, l and the isotopic mass difference on the local phase $\phi(E,l)$ at r_0 comes only from the WKB range, so that up to a constant

$$\phi(E,l) = \frac{1}{\hbar}\int^r p(r)\mathrm{d}r = \int^r \left[\frac{2\mu}{\hbar^2}(E-V) - \frac{l\,(l+1)}{r^2}\right]^{\frac{1}{2}} \mathrm{d}r. \tag{3.18}$$

Moreover, the small E and l ranges allow a first order Taylor expansion [25] for $\phi(E,l)$ yielding

$$\phi(E,L) = \phi_0 + E\left.\frac{\mathrm{d}\phi}{\mathrm{d}E}\right|_{l=0} + l(l+1)\left.\frac{\mathrm{d}\phi}{\mathrm{d}l(l+1)}\right|_{E=0}, \tag{3.19}$$

with

$$\left.\frac{\mathrm{d}\phi}{\mathrm{d}E}\right|_{l=0} = \int \frac{\mu \mathrm{d}r}{\hbar^2 k} \propto \sqrt{\mu} \tag{3.20}$$

$$\left.\frac{\mathrm{d}\phi}{\mathrm{d}l(l+1)}\right|_{E=0} = \int \frac{\mathrm{d}r}{2kr^2} \propto \frac{1}{\sqrt{\mu}}. \tag{3.21}$$

By making use of this method we introduce two (S=0,1) times three (ϕ_0, ϕ_E, and ϕ_l) parameters which have to be determined by comparison of theoretically predicted to experimentally determined properties of cold collisions. In our fit we use $r_0 = 16a_0$ (see section 3.6). Up to this radius the singlet potential is accurately known (see section 3.3, [22]) so that we do not have to apply the accumulated phase method to eliminate uncertainties in this potential. The parameters $\phi_0, \phi_{E,S}, \phi_{L,S}$ can therefore be calculated. The triplet potential is not known accurately enough up to $r = 16a_0$ and we are left with a total of three unknown parameters to characterize the inner part of the triplet potential. The analysis in which these three parameters are deduced from experiments is outlined in chapter 4 and results can be found in table A.3.

Mass scaling

As can be seen from eqs. (3.18) and (3.20) the phase parameters are mass dependent implying we would need a total of six parameters for a description

of ^{85}Rb and ^{87}Rb experiments. However Seto *et al.* [21] have been able to describe ^{85}Rb and ^{87}Rb interactions within a precision of $0.001\text{cm}^{-1} \approx 30\text{MHz}$ (up to $r = 25a_0$) with a common potential. The fact that there is a common potential for the isotopes means that we can relate the parameters for these different isotopes by mass scaling.

From eqs. (3.20) it is clear that ϕ_E and ϕ_l should be mass scaled as

$$^{85}\phi_E = \mathcal{R}\ ^{87}\phi_E \qquad \text{and} \qquad ^{85}\phi_l = \mathcal{R}^{-1}\ ^{87}\phi_l, \tag{3.22}$$

with $\mathcal{R} = \sqrt{m_{85}/m_{87}}$, in which m_x is the mass of ^{x}Rb.

The mass scaling for ϕ_0 deviates a little from the above equations due to a mass independent contribution to the accumulated phase of $\pi/4$ arising from the start-up of the wave function. Whereas for the boundary condition (i.e. the phase supplied in the calculations) the accumulated phase ϕ_0 may be given modulo π, it is of importance for the mass scaling to know the total phase. Since each 'modulo-π phase-cycle' equals one additional (vibrational) bound state in the potential we can express the total accumulated phase as $\phi_0 = n'_b\pi + \phi_{0,\pi}$, with n'_b the number of vibrational nodes up to the radius of interest (r_0) and $\phi_{0,\pi}$ the modulo-π part of the total phase. Given the $k \propto \sqrt{m}$ behavior, the scaled $^{85}\phi_{0,\pi}$ becomes

$$^{85}\phi_{0,\pi} = \mathcal{R}\ ^{87}\phi_{0,\pi} + (1-\mathcal{R})\frac{\pi}{4} - {}^{85}n'_b\pi + \mathcal{R}\ ^{87}n'_b\pi. \tag{3.23}$$

The last term gives rise to a number of discrete values for the mass-scaled phase depending on the number of nodes (up to r_0) contained in the potential. The interval between these discrete values is approximately $(1-\mathcal{R})\pi \approx 0.012\pi \approx 0.036$. A change of this order in the accumulated phase gives rise to an enormous change in the predicted values for the quantities to be fitted (see chapter 4). The performed analysis yields $\chi^2 = 0.5$ for the number of nodes (up to r_0) which are found to be correct and a $\chi^2 = \mathcal{O}(10^3)$ if this number deviates by one. This implies that we are able to deduce the number of nodes contained in the potential up to r_0 and thereby the total number of bound states contained in the complete potential.

3.5 The scattering process

Phase shift introduced by scattering

In this section the elastic scattering between two atoms is considered. To simplify the picture we will only take into account the central interaction potential and describe the relative motion of the atoms. A movement towards the scattering region can be written as a wave function moving in the z-direction with momentum $\hbar k$: $\psi_{inc} = \exp(ikz)$.

Since we are considering a central force problem there is spherical symmetry and we expect no dependence on the polar angle. After scattering the wave function can therefore be denoted by $\frac{f(\theta)\exp(ikr)}{r}$ (with $f(\theta)$ the scattering amplitude and θ the azimuthal angle) yielding the asymptotic expression

$$\psi = \psi_{inc} + \psi_{scatt} \sim e^{ikz} + \frac{f(\theta)e^{ikr}}{r}, \tag{3.24}$$

with $k = \sqrt{2\mu E}/\hbar$ (the mutual potential energy is zero at very large separations). In the region where the interaction potential is not zero we must solve the Schrödinger equation to obtain the wave function. The Schrödinger equation for a central potential $V(r)$ problem of a system with mass μ is

$$\left[\frac{-\hbar^2}{2\mu}\nabla^2(\vec{r}) + V(r)\right]\psi(\vec{r}) = E\psi(\vec{r}). \tag{3.25}$$

With $k^2 = 2\mu E/\hbar^2$ and $U(r) = 2\mu V(r)/\hbar^2$ we can rewrite the Schrödinger equation to $[\nabla^2 + k^2 - U(r)]\psi(\vec{r}) = 0$. Recalling the spherical symmetry and substituting $\psi(r,\theta) = \frac{u(r)}{r}Y(\theta)$ in the last equation we can separate into two differential equations. One for the angular part with Legendre polynomials, P_l, as solution. A second one for the radial part. We can write down a general solution [26]

$$\psi(\vec{r}) = \frac{1}{r}\sum_{l=0}^{\infty} A_l u_l(r) P_l(\cos\theta), \tag{3.26}$$

which is called *the partial wave expansion*, with $u_l(r)$ the solution of the radial differential equation (3.27). The choice for A_l must be such that (3.26) represents the sum of an incoming plane wave and an outgoing spherical scattered wave. The differential equation for the radial part is given by

$$\left[\frac{\mathrm{d}^2}{\mathrm{d}r^2} + k^2 - U_l(r)\right]u(r) = 0, \tag{3.27}$$

with $U_l(r) = U(r) + \frac{l(l+1)}{r^2}$ the central potential plus a centrifugal barrier. At large interatomic separation $U_l(r)$ will be negligible and the solution to eq. (3.27) is $\sin(kr + \delta_l)$. We define the solution, however, to be

$$u_l(r) \sim \frac{1}{k}\sin\left(kr - \frac{l\pi}{2} + \eta_l\right), \tag{3.28}$$

such that the *phase shift* η_l will be zero if $U(r)$ is zero.

Substitution of (3.28) in eq. (3.26) yields the asymptotic form of the wave function

$$\psi(r) \sim \frac{1}{kr}\sum_{l=0}^{\infty} A_l \sin\left(kr - \frac{l\pi}{2} + \eta_l\right) P_l(\cos\theta), \tag{3.29}$$

which must be the same as eq. (3.24). Expanding e^{ikz} and $f(\theta)$ as a summation over Legendre polynomials ($z = r\cos\theta$) we can find [26]

$$f(\theta) \;=\; \frac{1}{2ik}\sum_{l=0}^{\infty}(2l+1)(S_l(k)-1)P_l(\cos\theta), \tag{3.30}$$

with $S_l(k) = e^{2i\eta_l}$ the S-matrix element. The $S_l(k)$-term arises from the interatomic potential and the -1 following this term is the contribution from the unscattered incident wave. Equation 3.30 requires $A_l = i^l(2l+1)e^{i\eta_l}$.

To illustrate how the phase shift arises we consider the solutions of (3.27) in the case of s-wave collisions (i.e. l=0). These solutions are

$$\begin{matrix}\sin(kr)\\ \cos(kr)\end{matrix}\ . \tag{3.31}$$

Only the $\sin(kr)$ gives a regular solution at the origin since the radial function of ψ is $u(r)/r$. In absence of a scattering potential $u(r)$ must therefore be $\sin(kr)$. In presence of a scattering potential the solution must still be regular at the origin but at very large separations we now may also have the $\cos(kr)$-term and this solution must be matched to the solution which evolved from the origin in the presence of the potential. The general solution at large separations can be written as

$$c_1 \sin(kr) + c_2 \cos(kr) = c \sin(kr + \eta_0). \tag{3.32}$$

In absence of a potential $\eta_0 = 0$ and we only have the incoming wave at large separations. The presence of the potential thus introduces a phase η_0.

The absolute value of the scattering amplitude can be expressed as

$$|f(\theta)|^2 = I(\theta) = \frac{1}{k^2} \left| \sum_{l=0}^{\infty} (2l+1) e^{i\eta_l} \sin \eta_l P_l(\cos\theta) \right|^2 . \tag{3.33}$$

To obtain the scattering cross-section σ we have to integrate $\mathrm{d}\sigma/\mathrm{d}\Omega$ which equals [26] $I(\theta)$ over the complete solid angle Ω, yielding

$$\sigma = \frac{4\pi}{k^2} \sum_{l=0}^{\infty} (2l+1) \sin^2 \eta_l. \tag{3.34}$$

Until now we have not taken into account the symmetrization requirement for identical particles. The boson symmetrization requirement puts in an extra factor of 2 in equation (3.34) [27] replacing 4π by 8π and the sum must be taken over *even* values l only.

Scattering length and the v_D quantum number

The scattering length a is defined to be [28]

$$a \equiv - \lim_{k \to 0} \frac{\tan[\eta_0(k)]}{k}, \tag{3.35}$$

which can be interpreted as a hard-sphere radius. At short range the wave function undergoes many oscillations due to the inter atomic potential. At large separations the wave function is proportional to $\sin(kr + \eta_0) = \sin[k(r - a)]$. This is a translation over a distance a compared to the case of no interaction at all (see figure 3.8) and represents the case of a hard wall at $r = a$.

The scattering length is thus an important property in the description of cold collisions. The magnitude of the scattering length is determined by the position of the last bound state. Knowledge of the position of this last bound state is therefore desirable for determining the long range interaction potential. The relation between the last bound state and the scattering length is illustrated in the figures 3.9 and 3.10.

In figure 3.9 the scattering length is plotted versus the depth of the potential. In this figure a model potential $V(r)$ is used. Its depth is varied by multiplication by $(1 + \lambda)$. Figure 3.10 shows the radial wave functions $u_0(r)$ for three different potential depths. For clarity the depth is strongly reduced to such values that the first bound state is just available in the second graph. This figure also

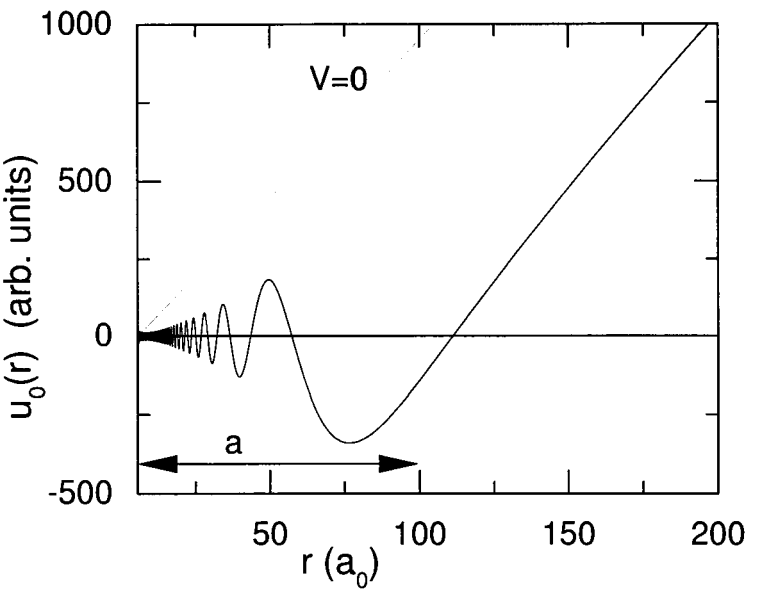

Figure 3.8: Radial scattering wave function $u_0(r)$ for very low energies (1nK) in the case of no interaction potential ($V = 0$) and in case of singlet interaction potential (^{87}Rb). Both have the same asymptotic behavior but the latter is displaced by the interaction potential over a distance a called the scattering length.

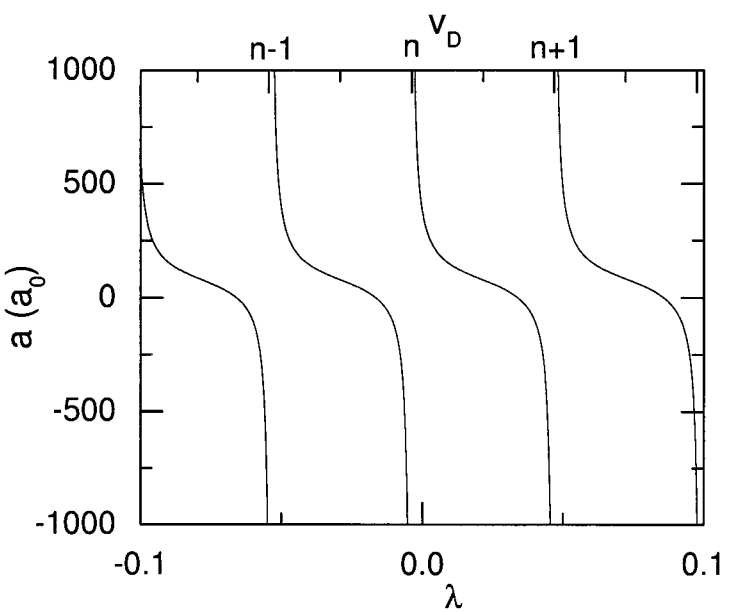

Figure 3.9: Scattering length as a function of the potential depth. A model potential $V(r)$ is used which is adjusted according to $(1 + \lambda)V(r)$. The upper axis denotes v_D, the fractional vibrational quantum number at dissociation, which is integer (n is an integer) at the depths where a new bound state is supported by the potential.

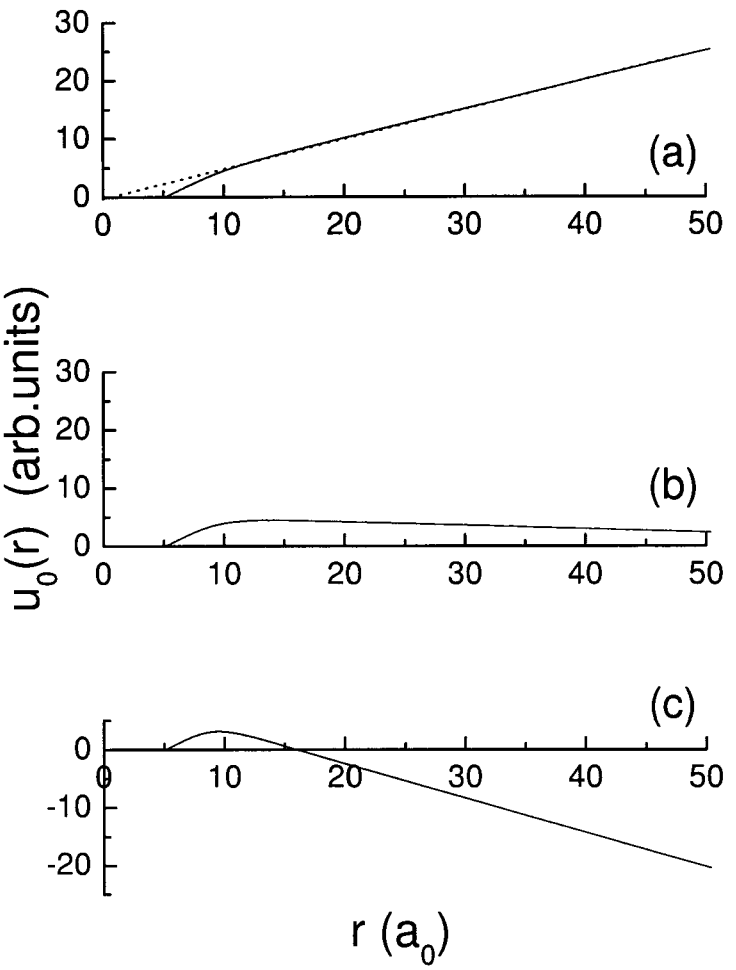

Figure 3.10: Behavior of the wave function $u_0(r)$ as a function of the potential depth. The Rb singlet potential is multiplied by λ' which is 10^{-5}, $2.5 \cdot 10^{-5}$, and $5 \cdot 10^{-5}$ for the graphs (a), (b), and (c) respectively. Just as in figure 3.8 we can extrapolate the nearly linear behavior in the long range to find its crossing with the r-axis which equals the scattering length a. From the graphs we can clearly see that a must go through infinity at the point where the deepening potential crosses the depth at which it can support one extra bound state. When the scattering length equals $+\infty$ the linearly behaving wave function crosses the r-axis at $+\infty$ and that extra node in the wave function represents one extra bound state. This also shows the dependence of the scattering length on the position of the last bound state. *For clarity and easy comparison the separate graphs are drawn on the same scale vertically and horizontally therefore the zero crossing in (b) lies outside the graph:* $a \approx 90a_0$

illustrates the correlation of the position (depth) of the last bound state and the scattering length.

For inelastic collisions the internal quantum state of one or both of the ingoing atoms changes during the collision and exits the collision in another quantum state leading to a complex valued η_0 (in case of multiple open channels $|S_0| < 1$ for the entrance channel: $|S_0|e^{i\varphi_{S_0}} = e^{2i\eta_0}$). In such a case we can define a complex scattering length in which the imaginary part represents a damping of the scattering amplitude corresponding to losses in the entrance channel (the atom has another quantum state after the collision) [29]

$$S_0 = e^{2k\Im(a)} \cdot e^{-i2k\Re(a)}. \tag{3.36}$$

It follows that

$$\Re(a) = -\frac{\tan^{-1}\left(\frac{\Im S_0}{\Re S_0}\right)}{2k} \tag{3.37}$$

$$\Im(a) = \frac{\frac{1}{2}\ln\left[(\Re S_0)^2 + (\Im S_0)^2\right]}{2k}. \tag{3.38}$$

Note that the imaginary part of the scattering length may not be positive for the S-matrix element to be equal to or smaller than 1, which is demanded by conservation of flux, see also equation (3.30).

A quantum number used in practice is the fractional vibrational quantum number at dissociation v_D. This number indicates the number of bound states contained by the potential including the fractional piece of bound state contained in the energy interval bounded by the highest true bound state ($E_n < 0$) and the energy at infinite large separation of the two atoms (E=0=asymptotic energy of the potential). As the potential is lowered to contain one additional bound state, v_D becomes integer at the point where the next bound state enters the potential. Accordingly it can be related to the phase shift η_0 and the scattering length a. See figure 3.9 for an illustration of v_D.

In contrast to most of the literature on the subject we define v_D as a linear function of the phase ϕ_0, fixing the coefficients in the linear expression by equating v_D to the actual v value of a vibrational level when that is actually at zero energy. This is a natural way of interpolating between the integer v values, that avoids the near-dissociation quantum effects which lead to the more complicated relation between the integer part of v_D and the number of bound states pointed out by Boisseau et al. [30]. In our case we have simply

$$n_b = \text{entier}(v_D) + 1. \tag{3.39}$$

3.6 Coupled channels calculations

As we have seen in section 3.5 we can deduce the properties of colliding atoms from the S-matrix. To obtain the S-matrix we perform so-called coupled channel calculations (see e.g. [29]) in which all interactions described in section 3.2 are taken into account, except for V^{ss} which are taken into account optionally. In these calculations the channels are integrated starting in the classically forbidden area up to a certain separation where they are matched to the radially inward integrated channels (all channels are first expressed in the same basis). The S-matrix is constructed in the matching process.

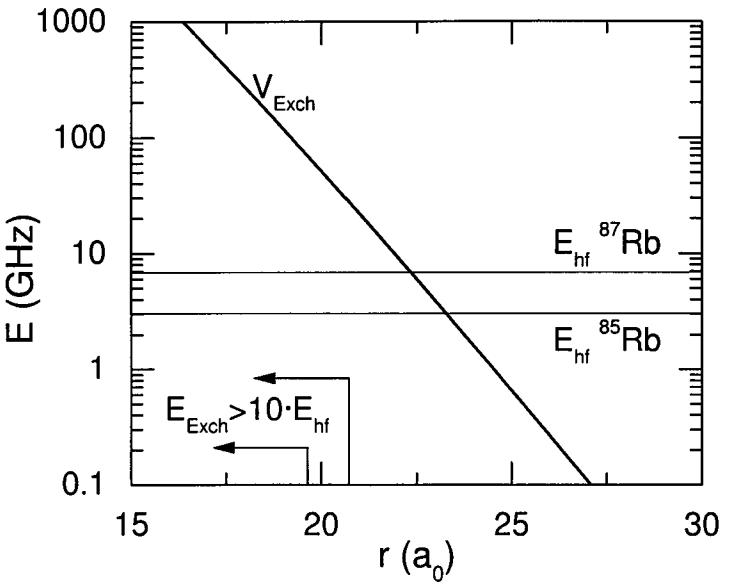

Figure 3.11: The exchange energy for two interacting Rb atoms. Indicated are the hyperfine energy for the two isotopes used in our analysis: 3.04GHz for ^{85}Rb and 6.83GHz for ^{87}Rb. The arrows (upper for ^{85}Rb) indicate the domain where V^{hf-} is expected to be adiabatic.

It can be shown (e.g. [15]) that V^{hf-} is the only interaction which couples singlet and triplet states. Therefore we can expect the coupling between these states to be negligible if the splitting between these states ($2V_{exch}$) is large compared to the energies of the hyperfine interaction (E_{hf}). In figure 3.11 the energies involved are plotted versus the interatomic separation. The region where we expect the coupling between singlet and triplet to be negligible is indicated by arrows, the upper one for ^{85}Rb and the other for ^{87}Rb.

For separations smaller than $16a_0$ we are in the region of negligible singlet-triplet coupling and the dynamics of the spin system is not coupled to the dynamics of the spatial system [15]. We speak of singlet and triplet channels. These channels stay decoupled up to a separation r_c where V^{hf-} is no longer negligible.

For large separations the interactions between the atoms are negligible. The channels are now constructed from (anti-)symmetrized products of single atom hyperfine states.

If at very large separations of the atoms the kinetic energy for a specific channel becomes negative (k imaginary) we will call these channels *closed*. Channels with a positive kinetic energy at very large atomic separations will be called *open*.

3.7 Feshbach resonances and shape resonances

What is a Feshbach resonance?

In the following we will meet two types of scattering resonances: *shape resonances* and *Feshbach resonances.* In a time-dependent picture based on the scattering of wave packets, such resonances show up as quasibound states into which part of the probability flux is captured during the scattering process and again released after a characteristic time, the resonance lifetime.

A shape resonance is the resonance type that is easiest to understand. They arise when a quasibound state occurs inside the centrifugal barrier for partial waves with $l > 0$ and they arise always in a single channel scattering process. The quasibound state would be truly bound (lifetime ∞) in the limit of an inpenetrable barrier. Figure 3.4 demonstrates a g-wave ($l = 4$) shape resonance that actually occurs in the experiments on ^{85}Rb that we are going to analyze.

In contrast, Feshbach resonances occur in a situation of coupled channels with more than one internal state of the collision partners. We can divide the space of all possible channels playing a role in a certain collision in two subspaces, a $\mathcal{P}$- and a $\mathcal{Q}$-space containing the *open* and *closed* channel internal states, respectively. We can distinguish Feshbach resonances into two types: *single open channel* Feshbach resonances and *multiple open channel* Feshbach resonances.

Both types of Feshbach resonance occur when there is a resonant coupling between the incoming wave and a bound state from $\mathcal{Q}$-space, becoming available by e.g. tuning the magnetic field. In this situation the wave cannot exit in the channel to which the bound state belongs. We can interpret this type of resonance as a transition of the incoming wave to the $\mathcal{Q}$-space, propagation in $\mathcal{Q}$-space, and a transition back to $\mathcal{P}$-space.

As mentioned above, resonances in which only one open channel is available for the quasibound state to decay into are called single open channel Feshbach resonances. In these resonances only one open channel, the incoming channel, plays a role. The field of this type of Feshbach resonances has already been explored to a large extent. Some properties will be discussed below. In chapter 4 we predict four resonances of this type for ^{87}Rb + ^{87}Rb scattering. These resonances are currently searched for by many groups, for instance at the Amherst College (Massachusetts) and at the Max-Planck Institute (MPQ) at Garching.

Figure 3.12 illustrates the physical mechanism behind a cold atom Feshbach resonance. For a system consisting of two atoms infinitely far separated, one in a state $|\gamma\rangle$ and the other in a state $|\delta\rangle$, the total internal energy is denoted by $E_{|\gamma\delta\rangle}$ in the state $|\gamma\delta\rangle$. This energy will be a function of the magnetic field B and is simply the sum of the one atom internal energy states depicted in figure 3.1. From the discussion in section 3.2 we know that during a scattering the atoms can couple to all channels with the same $m_{\mathcal{F}}$. The line labelled $|b\rangle$ in figure 3.12 represents the total internal energy for a bound state with the same $m_{\mathcal{F}}$; i.e. a state with another set of quantum numbers as $|\gamma\delta\rangle$ has, representing a state which might be formed during a collision (not excluded by selection rules). At zero magnetic field this state is not accessible due to its excess internal energy. If, however, the magnetic field is increased to the value where $E_{|b\rangle}$ crosses $E_{|\gamma\delta\rangle}$, the $|b\rangle$ state *is* accessible without change of energy and a strong coupling to this state will occur, giving rise to a single channel Feshbach resonance. The

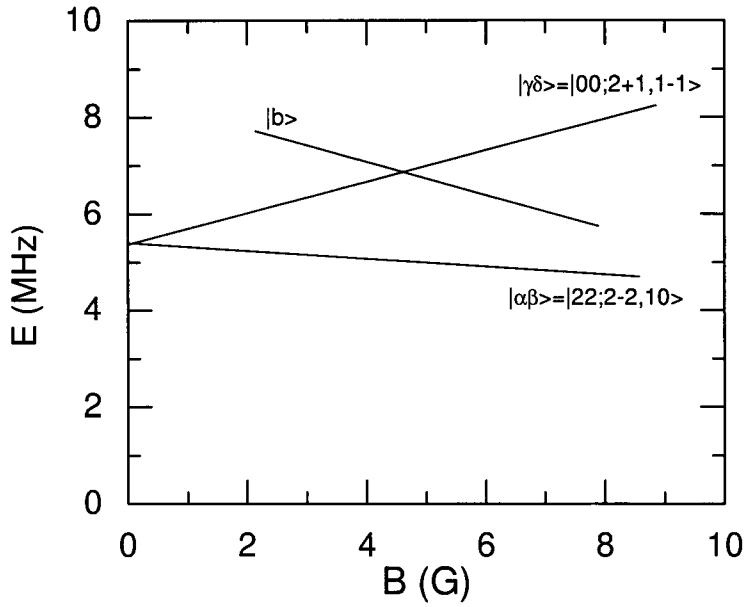

Figure 3.12: Energy of Feshbach resonances. Shown are the threshold to the continuum $|\gamma\delta\rangle$ (initial energy: $\varepsilon_\gamma + \varepsilon_\delta = E_{tot} - E_{kin}$) and the energy of a possible decay channel $|\alpha\beta\rangle$ ($m_\mathcal{F}$ conserved). The line labelled $|b\rangle$ represents a bound state. The resonance depicted here is a *multiple open channel resonance*, because $|\alpha\beta\rangle$ lies below the crossing point of E_b and the initial channel $|\gamma\delta\rangle$ threshold; otherwise it would have been a *single open channel* resonance.

graphs in figure 3.13 illustrate the increased coupling between channels in the neighborhood of a Feshbach resonance for ^{85}Rb.

Figure 3.12 illustrates at the same time a two open channel Feshbach resonance, when we assume that another open channel, here denoted by $|\alpha\beta\rangle$ with a threshold below the above-mentioned crossing point is available for the decay of the quasibound state. We will meet such resonances also in the following.

Moerdijk *et al.* have investigated the behavior of single open channel Feshbach resonances [31]. They derived the scattering length to be

$$a(B) = a^0(B) - \frac{C}{\varepsilon_{res}}, \tag{3.40}$$

in which a^0 is the background scattering length (i.e., the weakly B dependent scattering length without the presence of the resonance), C is a weakly B dependent parameter depending on the strength of the resonance, and ε_{res} is the actual resonance position relative to the threshold of the initial channel:

$$\varepsilon_{res}(B) = (\mu_i(B_0) - \mu_b(B_0))(B - B_0), \tag{3.41}$$

with $\mu_i(B)$ the sum of the single atom magnetic moments in the initial hyperfine states and $\mu_b(B)$ the magnetic moment of the two-atom resonance state. Substituting eq. (3.41) in eq. (3.40) we find

$$a(B) = a^0 - \frac{C}{2\mu_i(B_0) - \mu_b(B_0)} \frac{1}{B - B_0} \equiv a^0 \left(1 - \frac{\Delta}{B - B_0}\right), \tag{3.42}$$

which describes the typical behavior of the scattering length near a single open channel Feshbach resonance (see figure 3.14).

In the Phys. Rev. Letter presented in the following chapter we predict for the most frequently studied cold atom species ^{87}Rb not only the four above-mentioned single open channel Feshbach resonances, but also two multiple open channel Feshbach resonances. One occurs at 9.1G in the $|\gamma\delta\rangle = |(2,-1)(1,+1)\rangle$ cold atom channel, the other at 1.9G in the $|\gamma\delta\rangle = |(2,+1)(1,-1)\rangle$ channel. They were found by calculating the elastic scattering length as a function of the magnetic field following from coupled channel calculations. Numerically, they were precisely located by analyzing $a(B)$ and its first two derivatives.

The observation of all these Feshbach resonances at the predicted fields and with the predicted widths Δ constitutes a testing ground for our theoretical approach. Multiple open channel Feshbach resonances for cold atom scattering have not yet been observed experimentally and are also theoretically largely unexplored. Exploration of this new field is a partial subject of my future PhD research. There are strong indications that the 1.9G multiple channel Feshbach resonance has in the meantime been found experimentally by Cornell and coworkers [32] only a few weeks after our predictions. One interesting aspect, which still requires considerable effort for understanding, is that this resonance shows at the same time features of a Feshbach and of a shape resonance.

3.8 Practical aspects of the fitting

As mentioned several times before we perform a fit to determine the best values for parameters which characterize the interactions between colliding Rb atoms.

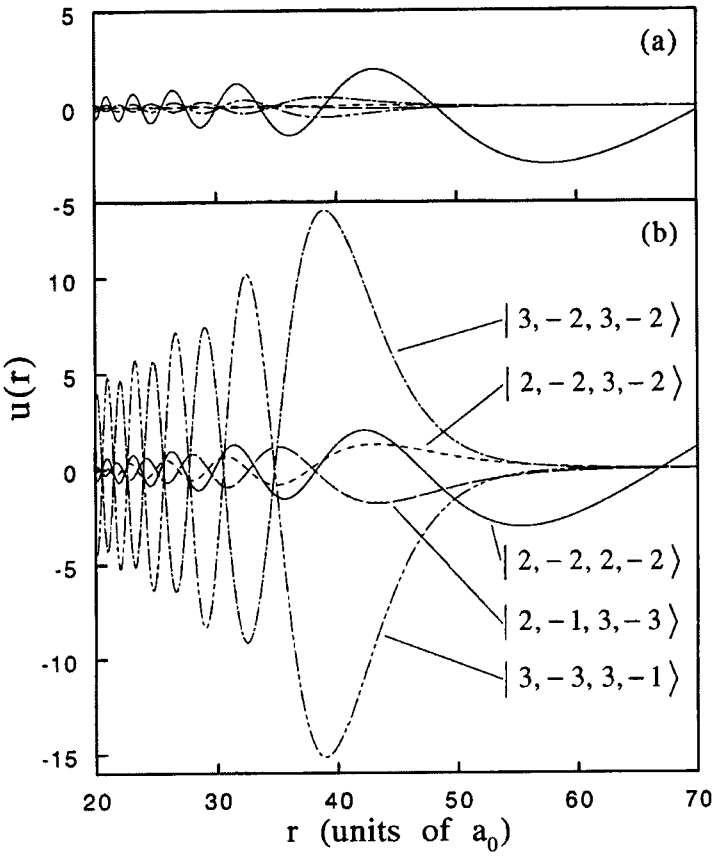

Figure 3.13: Behavior of the wavefunctions $u(r)$ near a Feshbach resonance. Due to the mechanisms described in section 3.2, a wave function in the entrance channel will couple to channels with the same $m_{\mathcal{F}}$. Shown are the wave functions of some channels with $m_{\mathcal{F}}$ equal to that of the entrance channel for two different magnetic fields. The upper graph is off-resonance, the lower graph is on resonance (see text). On resonance we see the strong coupling to the closed channels $|f_1, m_{f_1}; f_2, m_{f_2}\rangle = |3,-2;3,-2\rangle$ and $|3,-3;3,-1\rangle$. *The Feshbach resonance in this graph is not the same as the one than depicted in figure 3.12.*

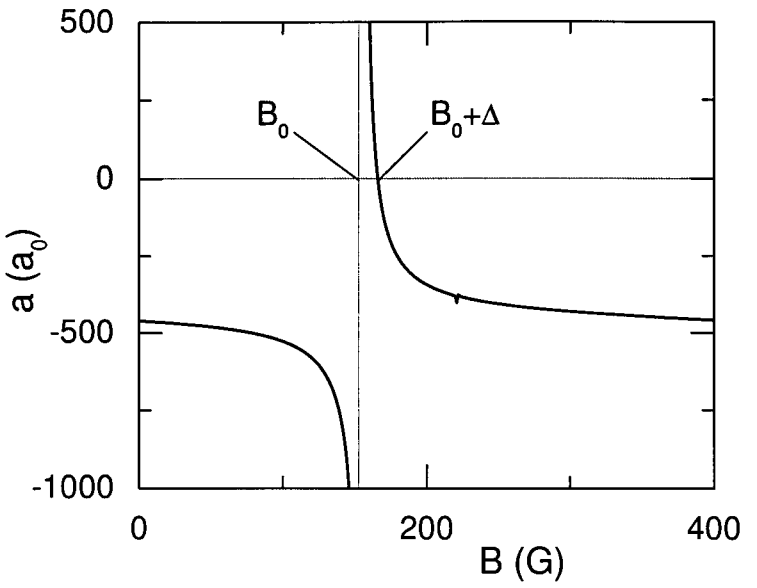

Figure 3.14: Typical behavior of the scattering length near a Feshbach resonance as function of the magnetic field. The Feshbach resonance depicted is the ^{85}Rb resonance used in our analysis.

We used a Marquardt-type routine to minimize χ^2 which we define by

$$\chi^2 = \sum_i (\chi^i)^2 = \sum_i \left(\frac{C^i_{exp} - C^i_{th}}{\sigma^i} \right)^2 , \tag{3.43}$$

with C^i_{th} the predicted value of a property i and C^i_{exp} the experimental value of this property which is known with a standard deviation σ^i.

Figure 3.15 shows a simplified overview of the program structure we use to perform the fit. The main program starts up the Marquardt routine with the best known values for the parameters $\phi_{T,0}$, $\phi_{T,E}$, $\phi_{T,L}$, C_6, C_8, J, C_{10}, and C_{11}; the last two optionally. The Marquardt routine passes interaction parameters to another routine which calculates the residue vector ($\underline{\chi}$) by calling the appropriate routines for calculating every C^i_{th}. In the χ^2-minimization process the Marquardt routine calls the residue routine several times, each time with other interaction parameters $\{\phi_{T,0}, \phi_{T,E}, \phi_{T,L}, C_6, C_8, J, C_{10}, C_{11}\}$(iter). Each time the residue routine is called, $\underline{\chi}(\{\phi_{T,0}, \phi_{T,E}, \phi_{T,L}, C_6, C_8, J, C_{10}, C_{11}\}$(iter)) is calculated, for which all the C^i_{th} routines have to be called. The Marquardt routine determines the χ^2 surface and gives as output the parameters at its (local) minimum, the standard deviations of these parameters, and the correlation matrix.

The different C^i_{th}-routines calculate energy levels, mixed-condensate decay rate, Feshbach resonance parameters, or the differences between the potentials defined by Seto *et al.* and the asymptotic approximation (eq. (3.4)).

The energy levels are calculated by solving the set of second-order coupled

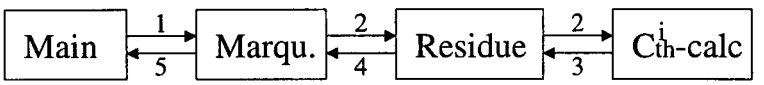

Figure 3.15: Schematic overview of program structure used for the fit. The arrows indicate the passing of: (1) initial interaction parameters; (2) interaction parameters; (3) C^i_{th}; (4) $\underline{\chi}$; (5) parameters at the (local) minimum of the χ^2-surface with their standard deviation and the correlation matrix.

equations [15]

$$\frac{\partial^2}{\partial r^2}\underline{\psi} = \frac{2\mu}{\hbar^2}\left(\underline{\underline{W}} - E\underline{\underline{I}}\right)\underline{\psi}, \tag{3.44}$$

where the coupling occurs between various spin states, with $W_{ij}(r) = V_{ij}(r) + \frac{\hbar^2}{2\mu r^2} l(l+1)\delta_{ij}$ and E the energy of the level; see [15].

The mixed-condensate decay rate is calculated by obtaining the relevant S-matrix. The decay rate can than be deduced by summing the probabilities for transitions to different decay channels [29]

$$G_{tot} = \sum_{\alpha\beta} G_{\gamma\delta\to\alpha\beta} = \sum \langle v\sigma_{\alpha\beta,\gamma\delta}(v)\rangle_{th} \tag{3.45}$$

in which $\sigma_{\alpha\beta,\gamma\delta}(v)$ can be calculated from the S-matrix by eq. (3.34) suitably generalized to a multiple channel situation; $\langle . \rangle_{th}$ indicates thermal averaging over the collision velocity $\vec{v} = \hbar\vec{k}/\mu$; the summation is over all possible decay channels (i.e. same $m_{\mathcal{F}}$ as the $\gamma\delta$-state and exothermal transition); see [29].

Two parameters B_0 and Δ characterize a single channel Feshbach resonance. The scattering length a goes through infinity at a magnetic field $B = B_0$ and 'holds opposite sign' in the region $B_0 < B < (B_0 + \Delta)$; see equation (3.42) and figure 3.14. We calculate the Feshbach resonance by determining $a(B)$ for three B values around the experimentally found B_0^{exp} and fit the analytic expression (3.42) to obtain B_0^{th} and Δ^{th}. Then it is checked that sign reversal occurs in $a(B_0^{th} \pm \xi)$. If sign reversal is not present $a(B_0^{th} + \xi_{B_0})$ is calculated with varying ξ_{B_0} until sign reversal occurs. The same procedure is applied for $a(B_0^{th} + \Delta^{th})$. The final '$C^i_{th}$' values (i.e. B_0 and Δ) are calculated taking the corrections ξ_{B_0} and ξ_Δ into account. The calculation for the difference of the potentials defined by Seto *et al.* and the asymptotic approximation is straightforward.

Chapter 4

Analysis of ultracold rubidium interactions

Inter-isotope determination of ultracold rubidium interactions from three high-precision experiments

E.G.M. van Kempen, S.J.J.M.F. Kokkelmans, D.J. Heinzen, and B.J. Verhaar
accepted for PRL, January 2002.

Combining the measured binding energies of four of the most weakly bound rovibrational levels of the $^{87}Rb_2$ molecule with the results of two other recent high-precision rubidium experiments, we obtain exceptionally strong constraints on the atomic interaction parameters in a highly model independent analysis. The comparison of ^{85}Rb and ^{87}Rb data, where the two isotopes are related by a mass scaling procedure, plays a crucial role. Using the consistent picture of the interactions that thus arises we are led to predictions for scattering lengths, clock shifts, Feshbach resonance fields and widths with an unprecedented level of accuracy. To demonstrate this, we predict two Feshbach resonances in mixed-spin scattering channels at easily accessible magnetic field strengths, which we expect to play a role in the damping of coherent spin oscillations.

4.1 Introduction

After the first realization of Bose-Einstein condensation (BEC) in a dilute ultracold gas of rubidium atoms[33], experiments with the two isotopes ^{87}Rb and ^{85}Rb further lead to an amazingly rich variety of BEC phenomena, ranging from the controlled collapse of a condensate with tunable attractive interactions[34] to the realization of an atomic matter wave on a microchip[35]. Because of the large number of groups that have started doing experiments with these atomic species and the growing complexity and subtlety of the planned experiments, there is a clear need for a more precise knowledge of the interactions between ultracold rubidium atoms in the electronic ground state, since these determine most of the properties of the condensate. For instance, despite a widespread interest, until now to our knowledge no experimental group has been able to

locate the predicted[36] magnetic-field induced Feshbach resonances that can be used to tune the interactions between ultracold ^{87}Rb atoms. Being able to switch on or off these interactions at will by a mere change of magnetic field may well be one of the main assets of matter waves compared to light waves in the new matter wave devices. In an atomic interferometry device, in particular, a nonlinear interaction between interfering waves may be introduced or eliminated by changing a field applied at the intersection point.

In this Letter, combining the results of three very recent high-precision observations, we come close to a complete and model-independent specification of the interaction properties of ultracold rubidium atoms. The fact that two isotopes ^{85}Rb and ^{87}Rb are involved in the measurements makes the constraints exceptionally strong and also increases the predictive power: the interaction properties of any other fermionic or bosonic isotope with mass number 82, 83, 84, or 86 are now known with about the same precision. Using mass scaling to relate the different isotopes we are able for the first time to deduce for each of the isotopes the exact numbers of bound Rb_2 states with total spin $S = 0$ (singlet) and 1 (triplet). As an illustration of the predictive power we predict two Feshbach resonances in mixed-spin scattering channels for ^{87}Rb at easily accessible fields that could lead to new time dependent phenomena in coherent spin oscillations and spin waves. There are numerous effects, such as spinor condensate energy differences, which are proportional to differences of scattering lengths. Because these differences are unusually small in Rb, the potentials must be very accurate to calculate them to reasonable accuracy.

4.2 Experimental data

The first of the three high-precision experiments is the recent measurement of four of the highest bound rovibrational levels of the $^{87}Rb_2$ molecule with 10 kHz precision[37]. The second experiment is the improved characterization[38] of the elastic scattering near a Feshbach resonance in ^{85}Rb, leading to a more precise determination of the resonance field $B_0 = 154.9(4)$ G and the nearby field strength $B_0' \equiv B_0 + \Delta = 165.85(5)$ G, where the scattering length goes through zero (Δ is the (elastic) resonance width). The third experimental ingredient going into our analysis is the measurement[21] of 12148 transition frequencies between $X^1\Sigma_g^+$ vibrational levels of the $(^{85}Rb)_2$, $(^{87}Rb)_2$, and $^{85}Rb^{87}Rb$ molecules, leading to a highly accurate singlet Rb + Rb potential[39]. Moreover, within the accuracy of this experiment a comparison of levels for the three studied isotopomers shows no sign of Born-Oppenheimer break-down effects, i.e., the observed levels agree with a simple radial Schrödinger equation containing a common singlet potential $V_S(r)$ and the reduced atomic mass. Calculation shows [40] that this justifies neglecting such effects also in our analysis.

4.3 Basic analysis

Theoretical background

This set of extremely precise measurements calls for a very careful construction of the interatomic total spin $S = 0$ and 1 potentials, depending on the interatomic separation r. We combine the singlet potential of Ref. [21] with a

long-range part equal to the difference $V_{disp} - V_{exch}$ of a dispersion term and an exchange term, starting at a variable radius r_S between 21 and 23.5 a_0 (1 a_0 = 0.529Å). The part $V_{disp}(r)$ includes C_6, C_8, C_{10} terms and retardation, while $V_{exch}(r)$ is assumed to be given by the asymptotic form $\frac{1}{2}Jr^{7/2\alpha-1}\exp(-2\alpha r)$, derived by Smirnov and Chibisov[14] for r values where the overlap of the electron clouds is sufficiently small ($\alpha = 0.554a_0^{-1}$, following from the ionization potential $\frac{1}{2}\alpha^2$ of the Rb atom in atomic units (au)).

The triplet potential is subject to a larger uncertainty. For its short range part an *ab initio* potential is usually taken. To get rid of this model dependence, we use the accumulated phase method[41]: the 'history' of the atom-atom motion is summarized by a boundary condition at an interatomic distance r_0, in the form of the phase $\phi_T(E,l)$ of the oscillating triplet radial wave function ψ depending on energy E and angular momentum l. Specifying $\phi_T(E,l)$ is equivalent to giving the logarithmic derivative ψ'/ψ at $r = r_0$. In all of our previous work we neglected the singlet-triplet mixing by the hyperfine interaction V_{hf} of the nuclear and electronic spins in the range $r < r_0$, in order to deal with pure singlet and triplet radial waves until the boundary. Here, however, we introduce a new variant that allows us to choose a larger r_0 than would otherwise be possible: we include the adiabatic mixing by V_{hf} in the two-atom spin states but still neglect its influence on the radial wave functions to avoid dependence on the history other than via the pure triplet phase. Model calculations show that in this form the scattering calculations have the required accuracy for r_0 values up to 16 a_0. The experimental data for either ultracold or weakly bound atoms that we analyze comprise a small E and l range near $E = l = 0$. In this range a first order Taylor expansion $\phi_T(E,l) = \phi_T^0 + E\phi_T^E + l(l+1)\phi_T^l$ is adequate, which reduces the information contained in $V_T(r)$ for $r < r_0$ to three phase parameters only. In principle, these would be needed for both the ^{85}Rb and ^{87}Rb systems. However, since we expect Born-Oppenheimer breakdown effects to be negligible also for the triplet channel in the distance range $r < r_0$, we use mass scaling to express $\phi_T^0, \phi_T^E, \phi_T^l$ for ^{85}Rb in terms of the three phase parameters for ^{87}Rb. Beyond r_0 we construct $V_T(r)$ from $V_S(r)$ by adding $2V_{exch}(r)$.

Used experimental data

Applying this method we carry out a full quantum scattering calculation for a set of eight experimentally measured quantities. This set consists of five quantities for ^{87}Rb and three for ^{85}Rb. The ^{87}Rb data are the four bound state energies and the ratio of scattering lengths $a_{1-1}/a_{21} = 1.062(12)$ for atomic scattering in condensates of ^{87}Rb atoms in the hyperfine states $(f, m_f) = (1,-1)$ and $(2,1)$ [42]. For ^{85}Rb we include the Feshbach resonance fields B_0 and B_0', as well as the energy 0.7(1) mK of the g-wave shape resonance observed in the scattering of a pair of cold atoms in the total spin $S = 1$ state[43].

The fit

With a least-squares search routine we determine optimal values for the parameters $C_6, C_8, J, \phi_T^0(^{87}\text{Rb})$, $\phi_T^E(^{87}\text{Rb})$, $\phi_T^l(^{87}\text{Rb})$. C_{10} is kept fixed at the value calculated by Marinescu *et al.* [12], but the effect of ±10% variations around this value and an estimated upper bound for the influence of higher dispersion terms are included in the final error bars. Column A of Table 4.1 summarizes

the main results of the calculations. We find a value for C_6 in agreement with the theoretical value 4691(23) obtained by Derevianko *et al.* [44]. The C_8 value agrees with that calculated by Marinescu *et al.*[12]. To our knowledge this is the first experimental determination of C_8 from a combined set of cold-atom + bound state data. Our analysis also yields the first experimental value of the strength of V_{exch} from such data. The coefficient J agrees with the most recent theoretical value in Ref. [45]. Table 4.1 also gives the values of the pure singlet and triplet scattering lengths for both ^{85}Rb and ^{87}Rb, following from $C_6, C_8, J, \phi_T^0(^{87}\mathrm{Rb})$, as well as the fractional vibrational quantum numbers at dissociation v_D(mod. 1) [41] and the numbers of bound states n_b. The reduced minimum χ^2 value is 0.5.

Predictions using the results

The foregoing makes clear that a major step forward has been made possible by the new experiments, two of which make use of a Bose-Einstein condensate. This is a firm basis for making a variety of interesting predictions. As a first example we predict the ^{87}Rb $f = 1$ spinor condensate to be ferromagnetic, i.e., it is favorable for two $f = 1$ atoms to have their spins parallel, because the mean field interaction is more repulsive for total $F = 0$ than for $F = 2$: the calculated scattering lengths are $a_{F=2} = +100.4(1)a_0$ and $a_{F=0} = +101.8(2)a_0$. In a recent preprint Klausen *et al.*[46] independently come to this conclusion of a ferromagnetic spinor condensate by calculating the scattering lengths for several assumed numbers of triplet bound states.

We are also able to predict collisional frequency shifts in an ^{87}Rb fountain clock for arbitrary choices of partial densities of atomic hyperfine states. Table 4.2 compares our calculated fractional frequency shifts normalized to total atom density n for two recent experiments[47, 48]. We find good agreement with the three measured shifts.

For various applications there is widespread interest for predictions of magnetic field values at which Feshbach resonances are to be expected in the scattering of two ^{87}Rb atoms in the $(f, m_f) = (1, +1)$ state. With our interaction parameters we expect them at the four resonance field values B_0 given in Table 4.3 together with the widths Δ. The B_0 values are to be compared with the values 383, 643, 850, and 1018 G predicted in 1997 [36]. It is interesting that the broadest resonance at 1004 G shows a doublet structure[40].

Figure 4.1 shows Feshbach resonances that we predict to occur in the mixed spin channels (2,+1)+(1,-1) and (2,-1)+(1,+1) at easily accessible field values of 1.9 and 9.1G, respectively. The graphs show the predicted field-dependent scattering lengths $a(B)$, which are complex functions due to the presence of exothermal inelastic decay channels. The generalized analytic expression for the field dependence in this case is[40]:

$$a(B) = a_\infty \left(1 - e^{2i\phi_R} \frac{\Delta_{el}}{B - B_0 + \frac{1}{2}i\Delta_{inel}}\right), \tag{4.1}$$

with Δ_{el} and Δ_{inel} the (in)elastic resonance widths and ϕ_R a resonance phase constant, arising due to inelasticity. Note that the real part of the scattering length does not go through infinity. It turns out that the 1.9G resonance is an $l = 2$ resonance, which couples via the spin-spin interaction V_{ss} to the s-wave

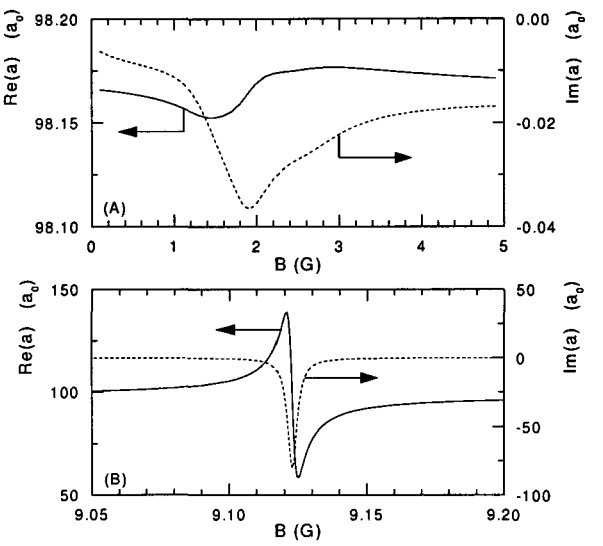

Figure 4.1: (A) Real (solid line) and imaginary (dashed line) parts of the scattering length $a(B)$ in s-wave ^{87}Rb (2,+1)+(1,-1) mixed spin scattering channel, showing the presence of a Feshbach resonance at 1.9G. Imaginary part is proportional to summed rate coefficient G for decay into all open channels. (B) Same for Feshbach resonance in (2,-1)+(1,+1) channel at 9.1G.

incident channel. Actually, this resonance is the 'hyperfine analog state'[40] in the (2,+1)+(1,-1) scattering channel of the d-wave shape resonance of ^{87}Rb occurring in the spin-stretched (2,+2)+(2,+2) spin channel[43], i.e., a state with essentially the same spatial dependence and differing only in its hyperfine spin structure[49]. It is located at a comparable low energy above threshold. In a similar way the $l = 0$ resonance at 9.1G is the hyperfine analog state of two of the $l = 0$ bound states observed[37] at roughly 25MHz below threshold in the (2,+2)+(2,+2) and (1,-1)+(1,-1) channels, belonging to the same rotational band as the d-wave shape resonance. They might play a role in the damping of coherent spin oscillations of the type which are being observed in experiments at JILA[32].

4.4 Extended analysis

Until now we assumed the expression for V_{disp} to be valid for interatomic distances larger than r_S. We now extend V_{disp} with C_{11} and C_{12} terms and assume it to be valid also between 18 a_0 and r_S. This leads us to a more ambitious approach that allows us to determine C_{10} and C_{11} as two more free parameters in the least squares search: we take into account the additional constraint arising from the equality $V_S(r) = V_{disp}(r) - V_{exch}(r)$ by imposing this equality at five r points as additional 'experimental data' with a standard deviation of 0.5%. We thus effectively include the bound states of Ref. [21] with outer

turning points in the range considered. In the search we take C_{12} equal to the theoretical value 11.9×10^9 of Ref. [13]. In column B of Table 4.1 the resulting optimal parameter values are given together with error bars based on a 25 % uncertainty in C_{12}. We find a value for C_{10} differing from the theoretical value 7.665×10^7 au [12] by only 1.8%. While the above attractive C_n terms with even n arise from the interatomic multipole-multipole interaction in second order, a C_{11} term is expected[50] as a repulsive third order dispersion term arising from the mutual dipole excitation and deexcitation of the atoms with an intermediate quadrupole transition between excited states in each of the atoms. Note that the ratio $C_{11}/C_{12} = -0.072$ is comparable to the rigorous value -0.028 for H atoms[51] and the *ab initio* ratio -0.041 for Cs atoms[52]. The remaining residue of the fit, concentrated at the smallest radii in the radial interval may well be due to the summed contributions of further (attractive and repulsive) dispersion terms beyond the C_{12} contribution plus correction terms to the Smirnov-Chibisov exchange expression. Note that the values of the lower dispersion coefficients are dominated by the close-to-threshold measurements, whereas the higher ones are determined primarily by the Seto potential in the middle range $r_0 < r < r_S$. We expect that experiment will prove the value of this more ambitious approach.

For completeness we point out that a weak contribution to the total atom-atom force is still missing in the above picture: the interatomic spin-spin interaction V_{ss}. One component of V_{ss} is the well-known magnetic dipole interaction between the valence electron spins of the interacting atoms. An additional contribution, which arises from the electronic spin-orbit coupling as a second-order effect, has been experimentally determined for the first time for rubidium atoms by Freeland *et al.*[37]. Calculation shows that V_{ss} has a negligible influence on the previous analysis.

4.5 Conclusions

In summary, combining the results of three recent high-precision experiments we have come close to a complete and model independent specification of the interaction properties of cold rubidium atoms. We have determined the van der Waals coefficients C_6, C_8, C_{10}, C_{11}, and the strength J of the exchange interaction. We have thus reached a consistent picture of the interactions, with which it is possible to predict essentially all parameters needed for a complete description of a rubidium Bose-Einstein condensate or thermal gas of any isotope in an arbitrary spin state. New experimental data, in particular on the Feshbach resonances, will undoubtedly be helpful to confirm the above consistent picture and to further narrow down the error limits. We believe that our approach sets an example for similar experimental and theoretical work for other (combinations of) atomic species. From a theoretical point of view, it is fascinating that it is possible to achieve a level of precision for the interaction properties approaching that for collisions of cold hydrogen atoms, based on a combination of experimental results and a sound framework of collision physics. Additional details and their relevance for future experiments will be the subject of a future publication[40]. We gratefully acknowledge the support of the work at Texas by the R.A. Welch Foundation, the US National Science Foundation, and the NASA Microgravity Research Division. The work at Eindhoven is part

of the research program of the Stichting FOM, which is financially supported by NWO.

4.6 Tables

Table 4.1: Interaction parameters (au) derived from experiments without (column A) and including (column B) the requirement $V_S = V_{disp} - V_{exch}$ for $r_0 < r < r_S$.

Quantity	A	B
$C_6/10^3$	4.703(9)	4.698(4)
$C_8/10^5$	5.79(49)	6.09(7)
$C_{10}/10^7$	7.665(Ref. [12])	7.80(6)
$C_{11}/10^9$	-	-0.86(17)
$C_{12}/10^9$	-	11.9(Ref. [13])
$J.10^2$	0.45(6)	0.42(2)
$a_T(^{87}\mathrm{Rb})$	+98.98(4)	+98.99(2)
$a_S(^{87}\mathrm{Rb})$	+90.4(2)	+90.0(2)
$a_T(^{85}\mathrm{Rb})$	-388(3)	-387(1)
$a_S(^{85}\mathrm{Rb})$	$+2795^{+420}_{-290}$	$+2400^{+370}_{-150}$
v_{DT}(mod. 1),$n_{bT}(^{87}\mathrm{Rb})$	0.4215(3), 41	0.4214(2), 41
v_{DS}(mod. 1),$n_{bS}(^{87}\mathrm{Rb})$	0.455(1), 125	0.456(1), 125
v_{DT}(mod. 1),$n_{bT}(^{85}\mathrm{Rb})$	0.9471(2), 40	0.9470(1), 40
v_{DS}(mod. 1),$n_{bS}(^{85}\mathrm{Rb})$	0.009(1), 124	0.011(1), 124

Table 4.2: Predictions of collisional frequency shifts for the ^{87}Rb fountain clock, compared to two recent experiments.

$\left(\frac{1}{n}\frac{\Delta\nu}{\nu}\right)_{exp}$ (10^{-24}cm^3)	Ref.	Present theory (10^{-24}cm^3)
-56^{+84}_{-21}	[47]	-72.5 ± 3.3
$-50(10)^{+22}_{-34}$	[48]	-32.8 ± 0.7
$-60(16)^{+29}_{-46}$	[48]	-41.5 ± 2.9

Table 4.3: Resonance fields B_0 and widths Δ for ^{87}Rb.

$B_0(G)$	403(2)	680(2)	899(4)	1004(3)
$\Delta(mG)$	< 1	15	< 5	216

Appendix A

Unit conversions and numerical values

Table A.1: Conversion factors between different energy units used in this thesis. Atomic units are denoted by E_H. Source: *http://physics.nist.gov/cuu/-Constants/index.html.*

Energy conversion factors

from\to	J	cm^{-1}	Hz	E_H	K
J	1	$5.034 \cdot 10^{22}$	$1.509 \cdot 10^{33}$	$2.294 \cdot 10^{17}$	$7.243 \cdot 10^{22}$
cm^{-1}	$1.986 \cdot 10^{-23}$	1	$2.998 \cdot 10^{10}$	$4.556 \cdot 10^{-6}$	1.439
Hz	$6.626 \cdot 10^{-34}$	$3.336 \cdot 10^{-11}$	1	$1.520 \cdot 10^{-16}$	$4.799 \cdot 10^{-11}$
E_H	$4.360 \cdot 10^{-18}$	$2.195 \cdot 10^{5}$	$6.580 \cdot 10^{15}$	1	$3.158 \cdot 10^{5}$
K	$1.381 \cdot 10^{-23}$	0.695	$2.084 \cdot 10^{10}$	$3.167 \cdot 10^{-6}$	1

Table A.2: Source: *http://physics.nist.gov/cuu/Constants/index.html.*

Numerical values constants

Symbol	Value	
h	$6.626 \cdot 10^{-34}$	Js
$\hbar$	$1.055 \cdot 10^{-34}$	Js
μ_B	$9.274 \cdot 10^{-24}$	JT^{-1}
μ_N	$5.051 \cdot 10^{-27}$	JT^{-1}
a_0	$0.529 \cdot 10^{-10}$	m
α_{fs}	$7.297 \cdot 10^{-3}$	

Table A.3: Numerical values for potential parameters either used in, or determined by, the analysis described in chapter 4. Values are in atomic units. Source: [a] Physica Scripta. Vol. 27, 300-305 (1983) [b] chapter 4.

Numerical values potential parameters

Symbol	Value	
α	0.5540877	[a]
${}^{87}\phi_{E,T}$	0.18415	[b]
${}^{87}\phi_{L,T}$	$-2.1342 \cdot 10^{-3}$	[b]

Appendix B

Technology assessment

The research presented in this thesis is a beautiful example of the interplay between experimental and theoretical work in physics, together leading to insights which will be useful for future technology. The experimental work (the measurement of four weakly bound states of Rb+Rb) used as input for the theoretical work, providing precise insight in the interactions between rubidium atoms. These insights can then again be used for prediction on the behavior of interactions between these atoms.

Insight in these interactions is of great practical importance. For example the locations (in magnetic field strength) of Feshbach resonances for ^{87}Rb+^{87}Rb predicted in this thesis give experimentalists a starting point for their search of these resonances (the Feshbach resonance in ^{85}Rb has only been found after the prediction of it's location).

Feshbach resonances can be used to tune the behavior of the interactions between atoms. Due to these resonances a simple change of the magnetic field strength can turn off (!) the interactions between a pair of atoms. A property which will prove to be valuable in e.g. atomic interferometers: one can switch off nonlinear interactions between interfering waves by changing the magnetic field. Instead of switching off the interactions between the atoms, a Feshbach resonance can also be used to increase the interactions between atoms: a property which can be used to shorten the time needed to Bose-condens a sample of atoms. This feature might improve atom lasers: either by simplifying Bose-condensation in a continuous steam of atoms[1] or by shortening the time intervals between pulses in a pulsed atom laser[2]

[1] To my knowledge this has not been demonstrated to work yet, but this idea is being pursued at ENS (Paris).

[2] One cycle in such an atom laser corresponds to the generation of a BEC from which atoms are extracted. Once the BEC is depleted, a new BEC has to be formed for the next pulse.

Bibliography

[1] W. Ketterle, D.S. Durfee, and D.M. Stamper-Kurn, Making, probing and understanding Bose-Einstein condensates, arXiv:cond-mat/9904034v2

[2] For an overview of groups in the world working with laser cooling and trapping, see: http://www.uibk.ac.at/c/c7/c704/ultracold/atomtraps.html. A site which only reports groups already having BEC, see: http://amo.phy.gasou.edu/bec.html.

[3] S.J.J.M.F. Kokkelmans, PhD thesis, Eindhoven University of Technology (2000)

[4] J.G.C. Tempelaars, PhD thesis, Eindhoven University of Technology(2001)

[5] R. Stas, Magnetic trap for BEC, master thesis, technische universiteit Eindhoven (1999).

[6] V. Mogendorff, Towards Ne* BEC, master thesis, technische universiteit Eindhoven (2000).

[7] H.J. Metcalf and P. van der straten, Laser cooling and trapping, Springer-verlag New York (1999).

[8] H. Beijerinck, P. van der straten, and H. Rudolph, Laserkoeling in theorie en praktijk, course syllabus, technische universiteit Eindhoven (1993).

[9] J. Opt. Soc. Am. B, v6 11 (1989), special issue: laser cooling and trapping of atoms.

[10] H.C.W. Beijerinck, E.J.D. Vredenbreght, R.J.W. Stas, M.R. Doery, and J.G.C. Tempelaars, Phys. Rev. A **61**, 23607-1 (2000).

[11] M.R. Doery, E.J.D. Vredenbreght, S.S. Op de Beek, H.C.W. Beijerinck, and B.J. Verhaar, Phys. Rev. A **58**, 3673 (1998).

[12] M. Marinescu, H.R. Sadeghpour, and A. Dalgarno, Phys. Rev. A **49**, 982 (1994).

[13] S.H. Patil and K.T. Tang, J. Chem. Phys. **106**, 2298 (1996).

[14] B.M. Smirnov and M.S. Chibisov, Zh. Eksp. Teor. Fiz. **48**, 939 (1965) [Sov. Phys. JETP **21**, 624 (1965)].

[15] J. Vogels, Master thesis, Eindhoven University of Technology, Netherlands (1996)

[16] M. Mizushima, The theory of rotating diatomic molecules (Wiley, New York, 1975) p. 233; P.S. Julienne et al. (priv. commun.)

[17] A.C. den Boer, Report 'Prestage' Theoretical Physics group, 7 July, 1992.

[18] F.H. Mies, C.J. Williams, P.S. Julienne, and M. Krauss, J. Res. Natl. Inst. Stand. Technol. **101**, 521 (1996).

[19] M. Kraus and W.J. Stevens, J. Chem. Phys. **93**, 4236 (1990)

[20] P.G. Hajigeorgiou R.J. Le Roy, J. Chem. Phys. **112**, 3949 (2000).

[21] J.Y. Seto, R.J. Le Roy, J. Vergés, and C. Amiot, J. Chem. Phys. **113**, 3067 (2000).

[22] J.Y. Seto, R.J. Le Roy, J. Vergés, and C. Amiot, J. Chem. Phys. **113**, 3067 (2000). *Direct potential fit analysis of the* $X^1\Sigma_g^+$ *state of* Rb_2*: Nothing else will do!*

[23] E.E. Nikitin and S.Ya. Umanskii, Theory of slow atomic collisions (Springer series in chemical physics; v. 30), Springer-Verlag, Germany (1984)

[24] A. Messiah, Quantum mechanics (North Holland Publishing Company, Amsterdam, 1961), Chapter XVIII, Section 14 and following.

[25] J.M. Vogels, PhD thesis, Eindhoven University of Technology (1999), pag. 37-56, spec. p. 44.

[26] J.N. Murrell and S.D. Bosanac, Introduction to the theory of atomic and molecular collisions, J. Wiley & sons, England (1989)

[27] E.W. McDaniel, Atomic collisions, J. Wiley & sons, U.S.A. (1989)

[28] Gordon W.F. Drake, Atomic molecular & optical physics handbook, USA (1996); this book contains references to the original sources.

[29] F.A. van Abeelen, PhD thesis, Eindhoven University of Technology (1999)

[30] C. Boisseau, E. Audouard and J. Vigué, Europhys. Lett. 41, 349 (1998).

[31] A.J. Moerdijk, B.J. Verhaar, and A. Axelsson, Phys. Rev. A **51**, 4852 (1995).

[32] E.A. Cornell (priv. commun.)

[33] M.H. Anderson *et al.*, Science **269**, 133 (1995); Press release Nobel prize in physics 2001 (www.nobel.se/physics/laureates/2001).

[34] J.L. Roberts *et al.*, Phys. Rev. Lett. **86**, 4211 (2001).

[35] W. Hänsel, P. Hommelhoff, T.W. Hänsch, and J. Reichel, Nature **413**, 498 (2001).

[36] J.M. Vogels *et al.*, Phys. Rev. A **56**, R1067 (1997).

[37] R. Wynar *et al.*, Science **287**, 1016 (2000); R.S. Freeland, D.Comparat, R. Wynar, C. Ryu, D.J. Heinzen, S.J.J.M.F. Kokkelmans, E.G.M. van Kempen, and B.J. Verhaar (to be published).

[38] J.L. Roberts *et al.*, Phys. Rev. A **64**, 024702 (2001).

[39] The analysis in Ref. [21] uses a pure C_6 dispersion tail at r values where our analysis shows higher dispersion terms to be significant. Calculation shows that this affects the derived singlet potential up to radii of about 23.5 a_0 to a negligible extent. Note that the transition frequencies define relative potential values only.

[40] E.G.M. van Kempen *et al.* (to be published).

[41] A.J. Moerdijk, W.C. Stwalley, R.G. Hulet, and B.J. Verhaar, Phys. Rev. Lett. **72**, 40 (1994); J.R. Gardner *et al.*, Phys. Rev. Lett. **74**, 3764 (1995).

[42] M.R. Matthews *et al.*, Phys. Rev. Lett. **81**, 243 (1998).

[43] H.M.J.M. Boesten, C.C. Tsai, B.J. Verhaar, and D.J. Heinzen, Phys. Rev. Lett. **77**, 5194 (1996).

[44] A. Derevianko, W.R. Johnson, M.S. Safronova, and J.F. Babb, Phys. Rev. Lett. **82**, 3589 (1999).

[45] G. Hadinger and G. Hadinger, J. Mol. Spectr. **175**, 441 (1996).

[46] N.N. Klausen, J.L. Bohn, and C.H. Greene, preprint arXiv:physics/-0104013.

[47] C. Fertig and K. Gibble, Phys. Rev. Lett. **85**, 1622 (2000).

[48] Y. Sortais *et al.*, Phys. Rev. Lett. **85**, 3117 (2000).

[49] A relation to the d-wave shape resonance was suggested to us by Eric Cornell.

[50] Y.M. Chan and A. Dalgarno, Mol. Phys. **14**, 101 (1968).

[51] J.F. Bukta and W.J. Meath, Mol. Phys. **27**, 1235 (1974).

[52] W. Weickenmeier *et al.*, J. Chem. Phys. **82**, 5354 (1985).